The Pennsylvania State University

The Graduate School

College of Engineering

PROTOTYPING AND OPTIMIZATION OF A MINIATURE MICROWAVE-FREQUENCY ION THRUSTER

A Thesis in

Aerospace Engineering

by

Mohammed Asif

© 2018 Mohammed Asif

Submitted in Partial Fulfillment
of the Requirements
for the Degree of

Master of Science

May 2018

The thesis of Mohammed Asif was reviewed and approved* by the following:

Sven G. Bilén
Professor of Engineering Design, Electrical Engineering, and Aerospace Engineering
Thesis Co-Advisor

Michael M. Micci
Professor of Aerospace Engineering
Thesis Co-Advisor

Amy Pritchett
Professor of Aerospace Engineering
Head of the Department of Aerospace Engineering

*Signatures are on file in the Graduate School

ABSTRACT

This thesis presents progress on the development of the Miniature Microwave-Frequency Ion Thruster (MMIT), currently being developed at Penn State as a microthruster with high specific impulse that can be used on small satellites for station keeping, attitude adjustments, and modest delta-V maneuvers. The MMIT works by generating a microwave electron cyclotron resonance (ECR) discharge plasma, then accelerating ions through a series of electrostatic grids. Using argon as the propellant, the MMIT can start with as low as 2.6 W of total absorbed power from a 4.98-GHz coaxial input power source. For the current MMIT iteration, our research thrusts have been threefold: demonstrating plasma generation; sustaining and containing the plasma; and extracting the ion beam. We have largely focused on optimizing the geometry of the magnets and antenna used for ECR plasma generation; defining the geometry of the chamber for containment of the plasma; and developing grid geometries for efficient beam extraction. Progress to date toward a functional prototype has leveraged numerical simulations and experimental measurements on the proof-of-concept design, which we are currently further optimizing. A Langmuir probe is used to measure ion density and temperature in the plume as well as beam current, and a Faraday cup is used to measure the current density of the beam. The measurements obtained from these probes are used as the basis for determining a calculated thrust for the MMIT.

TABLE OF CONTENTS

LIST OF FIGURES

LIST OF TABLES

LIST OF SYMBOLS

A	=	Effective area, m^2
A_e	=	Exhaust area of the nozzle, m^2
a	=	Radius of a cylindrical tube, m
$\vec{B}$	=	Magnetic flux density, T
B_0	=	Average flux density of a magnetic bottle, T
B_{max}	=	Maximum flux density of a magnetic bottle, T
$\vec{B}_r$	=	Residual magnetic flux density, T
C_p	=	Heat capacity at constant pressure, J $Kg^{-1}{\cdot}K^{-1}$
D	=	Diffusion coefficient
E_{ECR}	=	Energy gained by an electron in one cyclotron gyration, J
E_k	=	Kinetic energy of a single particle, J
E_p	=	Potential energy of a single particle, J
$\vec{E}$	=	Electric field strength, $V{\cdot}m^{-1}$
e	=	Elementary charge, 1.6×10^{-19} C
f	=	Frequency, s^{-1}
g_e	=	Acceleration due to gravity at Earth's surface, 9.81 $m{\cdot}s^{-2}$
$\vec{H}$	=	Magnetic field strength, $A{\cdot}m^{-1}$
I_b	=	Ion beam current, A
I_{sp}	=	Specific impulse, s
$\vec{J}$	=	Current density, $A{\cdot}m^{-2}$
J_b	=	Beam current density, $A{\cdot}m^{-2}$
J_o	=	Momentum out of the control volume, N
k_b	=	Boltzmann constant, 1.38×10^{-23} $J{\cdot}K^{-1}$
L	=	Distance between grids, m
l	=	Length of a tube, m
M	=	Atomic mass of the propellant, kg
m	=	Atomic mass of argon, 6.6335×10^{-26} kg
m_i	=	Initial mass of the propellant, kg
m_f	=	Final mass of the propellant, kg
$\dot{m}$	=	Mass flow rate, kg/s

$\dot{m}_{\mathrm{p}}$	=	Propellant mass flow rate, kg/s
N_{m}	=	Flow rate, mol·s^{-1}
n	=	Particle number density, m^{-3}
n_{e}	=	Electron number density, m^{-3}
P_{a}	=	Ambient pressure, Pa
P_{e}	=	Exhaust pressure, Pa
P_{in}	=	Total input electrical power, W
P_{jet}	=	Jet power, W
q	=	Elementary charge, 1.602×10^{-19} C
τ	=	Thrust, N
u_{e}	=	Exhaust velocity, m·s^{-1}
V	=	Potential difference between grids, V
Δv	=	Change in overall velocity, m·s^{-1}
Δv_{grav}	=	Change in velocity due to gravity, m·s^{-1}
Δv_{drag}	=	Change in velocity due to drag, m·s^{-1}
v_{e}	=	Exhaust velocity, m·s^{-1}
v_{eq}	=	Equivalent exhaust velocity, m·s^{-1}
ε_0	=	Permittivity in vacuum, 8.854×10^{-12} C
ζ	=	Viscosity of a fluid, Poise
η_{M}	=	Mass utilization efficiency
η_{E}	=	Electrical efficiency of a thruster
η_{M}	=	Mass utilization efficiency of a thruster
η_{T}	=	Total efficiency of a thruster
λ	=	Mean free path, m
λ_{D}	=	Debye length, m
μ	=	Mobility, m^2.V^{-1}.s^{-1}
μ	=	Magnetic moment, m^2·A
μ	=	Magnetic permeability of a generic medium, H·m^{-1}
μ_0	=	Magnetic permeability of vacuum, $4\pi \times 10^{-7}$ H·m^{-1}
μ_{r}	=	Mass utilization efficiency
σ	=	Cross section, m^2
σ	=	Electrical conductivity, S·m^{-1}

Φ	=	Degree of ionization of a gas
ω	=	Frequency of an electromagnetic wave, rad·s^{-1}
ω_c	=	Cyclotron frequency of a charged particle, rad·s^{-1}

ACKNOWLEDGMENTS

The journey towards the completion of this thesis has been graced with the contributions of several beings. I'd like to start by thanking Dr. Bilén and Dr. Micci for giving me the opportunity to be a part of their research team and support me throughout the project. I would also like to thank Pierre-Yves Taunay for his research on the previous iteration of the MMIT, which has been crucial to the developments made in this thesis. Thanks is also due to Jesse McTernan and Stephen Lovas for their technical advice and encouragement. Sang-Cheih Hsieh among others has been a supportive research partner. The most special thanks go to the two most important women in my life: my mother Saajitha Begum, and my significant other Yanan Xin.

Chapter 1

Introduction

Electric propulsion (EP) is of significant interest as an in-space propulsion technology. Chemical propulsion technology is relatively mature; however, more efficient in-space propulsion is needed, particularly for interplanetary travel. Given their higher specific impulses and considerable total impulse, EP has an edge over chemical propulsion for deep space missionrs.[1] Ion thrusters are increasingly being used as in-space propulsion devices. The miniaturization of these devices enables the application of this technology to various microspacecraft missions, which generally have constraints on power, mass, volume, and cost.

The concept of electric propulsion was first conceived by Robert Goddard in 1906. Tsilokoysky later independently wrote about electric propulsion in 1911, resulting in the development of the first electric thruster in 1929 by V.P. Glushko. The capabilities of EP were tested on various missions that took place during the space race between U.S. and U.S.S.R. in the 60s and 70s. JAXA[2–4] and ESA[5] established their research later in the 90s. However, technological constraints and other practical limitations played a role in the slower growth of EP research in comparison with chemical propulsion. Nevertheless, many government laboratories and universities have continued to research electric propulsion[6] and have flown some of these thrusters[7] on space missions.

1.1 Miniaturization of Electric Propulsion Devices

Ion thruster performance is limited by the power available for the system and miniaturization is a method to reduce the operating power of the thruster and the overall mass of the system. Almost every space mission is greatly limited by mass and power: the systems engineering approach to the thruster development requires less input power to ionize and accelerate the propellant and restricts the design considerations based on the mass and dimensions of the propulsion system.

1.2 Space Propulsion Research at Penn State

In recent years, development of this technology at the small scale has been directed toward potential CubeSat missions. This research and development includes the Miniature Microwave Ion Thruster (MMIT) at The Pennsylvania State University, which is being designed for station keeping, attitude adjustments, and modest delta-V maneuvers on small satellites.

Previous research on a small microwave discharge ion thruster by Koizumi and Kuinaka resulted in the development of the μ1 engine, which obtained an ion beam current of 3.3 mA using 1 W of input power and 0.15 sccm of xenon as propellant with 37% propellant utilization efficiency.[8] Their research was based on progress made by Takao et al.,[9–11] who described an ion engine with 72% propellant utilization efficiency, but using 8 W of input power at mass flow rates of 0.2 sccm of xenon.

Research on and development of miniature ion thrusters at Penn State began with Trudel's design of the 1-cm radio-frequency (RF) thruster (Figure 1-1) with propellant efficiency of 41% using 16 W of input power and 0.038 sccm of argon.[12,13] The operational parameters of the MRIT are shown in Table 1-1 and the test version of the MRIT is shown in Figure 1-2.

Table 1-1. MRIT Operational Parameters

Parameter	Nominal Value
Input frequency	1.5 MHz
Input RF power	16 W
Screen grid voltage	1000 V
Acceleration grid voltage	−200 V
Grid separation distance	0.14 in
Active grid diameter	1.0 cm
Propellant	Ar (99.999% purity)
Propellant flow rate	0.038 sccm
Specific impulse	2462 s
Thrust	64.8 μN
Total efficiency	20%
Mass utilization efficiency	41.1%
Electric efficiency	22.5%

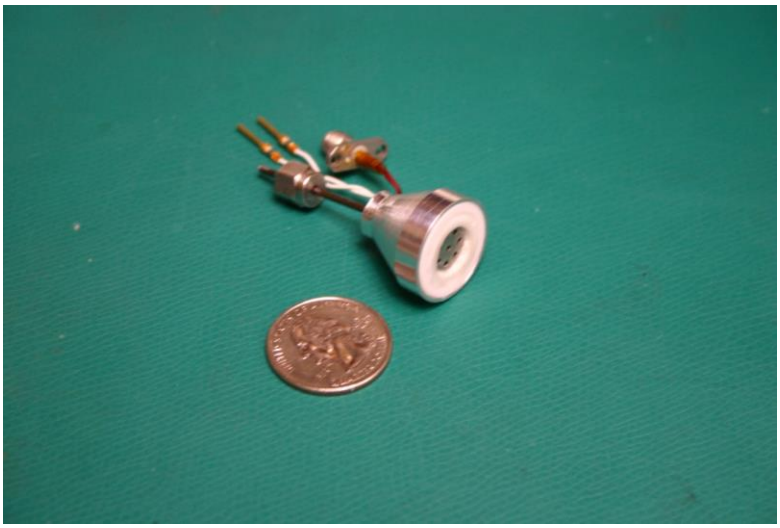

Figure 1-1. Trudel's MRIT compared to a U.S. quarter[12]

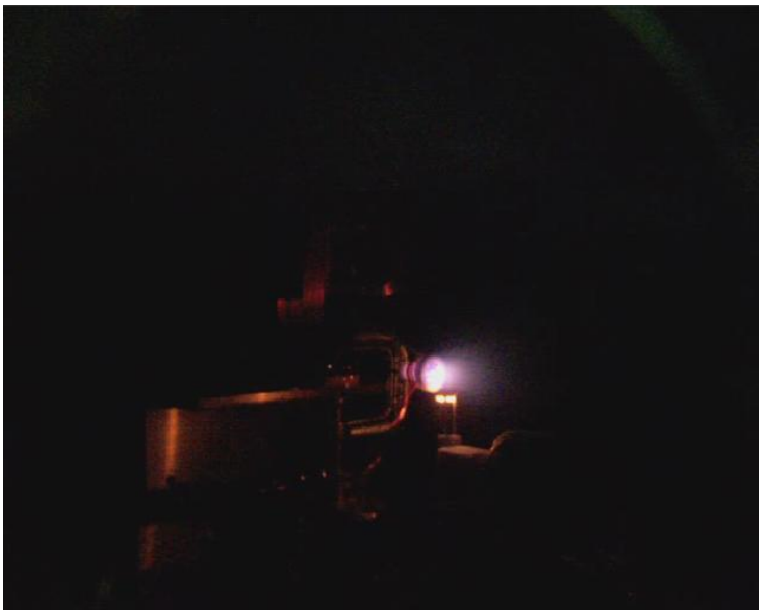

Figure 1-2. Trudel's MRIT operational test in a vacuum chamber[12]

Lubey refocused efforts from RF to microwave discharges, which resulted in the Miniature Microwave-Frequency Ion Thruster (MMIT)[14] shown in Figure 1-3. His design, based on JAXA's μ1 design, had theoretical estimated values of propellant utilization efficiency of 32% operating at 1 W power with a frequency of 4.2 GHz. Taunay redesigned the MMIT but used the same principle as the μ1, which resulted in a thruster with predictions of 217 μN thrust with 8 W total input power.[15,16]

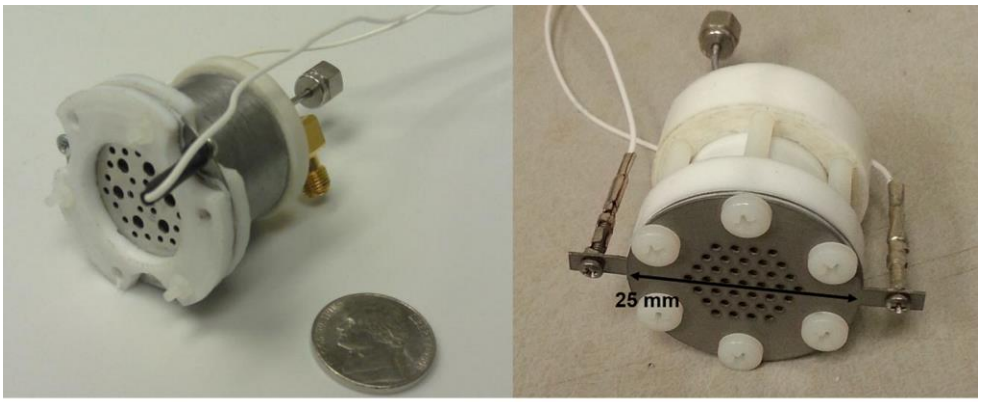

Figure 1-3. (a) Lubey's MMIT,[17] (b) Taunay's MMIT[15]

Both versions of the MMIT demonstrated plasma generation but were unable to demonstrate proper extraction of the ion beam shown in Figure 1-4 and Figure 1-5; however, theoretical estimates of thrust, specific impulse, and efficiencies were made through numerical simulations of the thruster design shown in Table 1-2. Their progress serves as the platform for the research presented in this thesis.

Figure 1-4. Lubey's MMIT operational test in a vacuum chamber[17]

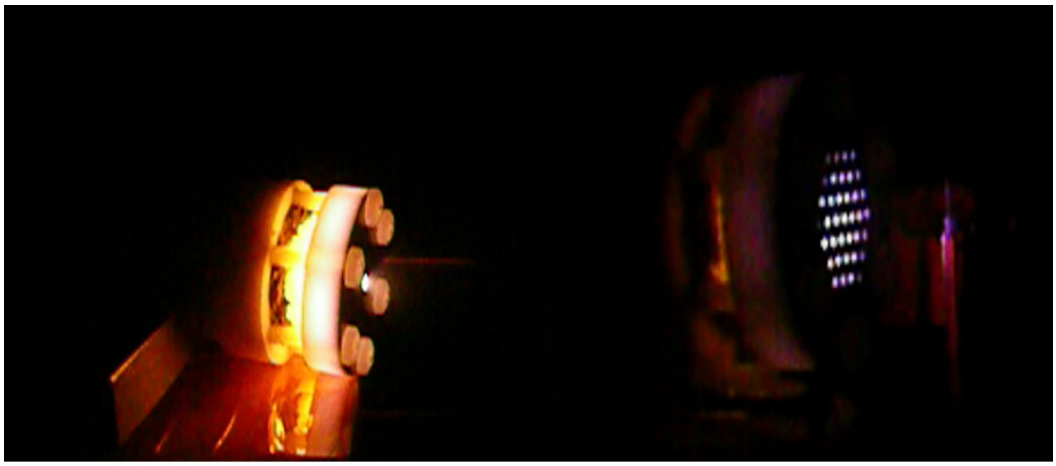

(a) (b)

Figure 1-5. Taunay's MMIT operational test in a vacuum chamber, (a) single-hole grid configuration, and (b) extraction grid configuration[15]

Table 1-2. Theoretical Predictions from the Previous MMIT Iteration

Parameter	**Theoretical Predictions**
Input frequency Input microwave power	4.2 GHz 1 W
Screen grid voltage Acceleration grid voltage Grid separation distance Active grid diameter	1500 V −500 V 0.02 in 1.0 cm
Propellant Propellant flow rate	Xe 0.15 sccm
Specific impulse Thrust	5540 s 258 μN
Total efficiency Mass utilization efficiency Electric efficiency	32.2% 32.1% 50.0%

1.3 Thesis Overview

This thesis presents progress on the development of the MMIT. Chapter 2 covers background information and equations for thrust. Chapter 3 covers the design changes and considerations employed for optimization. Chapter 4 describes the experimental facility and setup used in the experiments. Chapter 5 provides the experimental results from the current iteration of the thruster and issues faced. Chapter 6 summarizes the progress made towards the current MMIT iteration and possible future development paths for the thruster.

Chapter 2

Theoretical Background

This chapter overviews the basics of rocket propulsion with application to electric propulsion. An overview of the different types of propulsive devices are discussed with a more detailed presentation of the physics of electrostatic thrusters and the relevant physics needed to understand the functionality of the MMIT.

2.1 Spacecraft Propulsion

Spacecraft propulsion can be defined as any type of action that accelerates a spacecraft. There are two main roles: providing access to space and in-space propulsion. Acceleration using rocket engines is the most common type of space propulsion and currently the only effective method used to gain access to space. Rocket propulsion generates thrust by expelling mass from the system and it differs from air-breathing propulsion by the requirement to carry its own oxidant. Thrust is produced by satisfying Newton's third law of motion, which states that for every action, there is an equal and opposite reaction, both in magnitude and direction.

2.1.1 Tsiolkovsky Rocket Equation

Tsiolkovsky's equation, also known as the ideal rocket equation, is the governing equation for all rockets that exist today.[18] This equation is the result of applying conservation of momentum to a rocket and links the overall change in vehicle velocity to the exhaust velocity and mass fraction (ratio of propellant needed for the mission to the total mass of the rocket), i.e.,

$$\Delta v = v_{\mathrm{eq}} \ln \frac{m_{\mathrm{i}}}{m_{\mathrm{f}}} . \tag{2.1}$$

An important factor to consider in every space mission design is that manipulating any two of the variables makes the third variable become a fixed parameter.

To understand the significance of the ideal rocket equation, let's look at the conservation of momentum on the control volume of a rocket engine shown in Figure 2-1. For the sake of simplicity, we ignore the gravitational effects on the rocket engine.

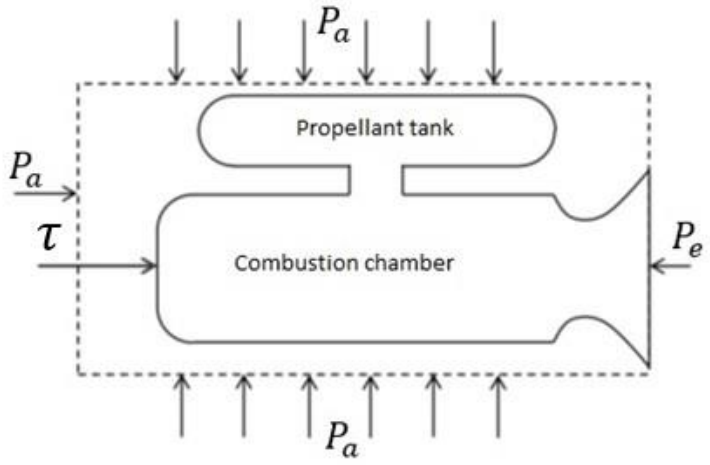

Figure 2-1. Forces on the control volume of a rocket engine[19]

Since momentum is conserved, the net forces acting on the control volume of this rocket engine must be equal to the change in momentum. There exists no inflow of momentum in rockets, hence the change in momentum is basically the momentum going out of the control volume,

$$J_{\mathrm{o}} = \dot{m} v_{\mathrm{e}} \,, \tag{2.2}$$

where $\dot{m}$ is the ejected mass flow rate and v_{e} is the exhaust velocity. This is commonly identified as thrust[20] and its integral over the entire mission is called total impulse. However, observing Figure 2-1 without the control volume and accounting for the continuous ejection of mass from the nozzle, we can say that a pressure field is created at the point of ejection causing a force to act on the system. This new force will change the considerations for the conservation of momentum.[21] This is the reason why we define the momentum with exhaust velocity and introduce a new term called equivalent exhaust velocity in the ideal rocket equation:

$$v_{\mathrm{eq}} = \left(\frac{P_{\mathrm{e}} - P_{\mathrm{a}}}{\dot{m}}\right) A_{\mathrm{e}} + v_{\mathrm{e}} \,. \tag{2.3}$$

This equation is the ideal rocket equation; the first term accounts for the pressure field. The force created is the difference in the exhaust pressure P_{e} at the nozzle and the pressure outside the system P_{a} acting over the cross-sectional area of the exit nozzle A_{e}.

The force that is being imparted on the vehicle by the rocket engine can be defined as thrust,

$$\tau = J_{\mathrm{o}} + (P_{\mathrm{e}} - P_{\mathrm{a}})\, A_{\mathrm{e}} = \dot{m} v_{\mathrm{eq}}. \tag{2.4}$$

It can be derived directly from the control volume or seen as the forces acting to influence the vehicle's motion. In this case, we have the pressure field at the nozzle and the ejection of mass. If we rewrite Equation (2.4) to account for the gravitational effect of the earth, then we get one of the most important parameters in rocket design, the "specific impulse", written as

$$I_{\mathrm{sp}} = \frac{\tau}{g\dot{m}} = \frac{v_{\mathrm{eq}}}{g}\,, \tag{2.5}$$

which is the ratio between the thrust produced by the engine and the mass flow rate of the propellant from the system. Equation (2.5) is the measure of how effectively the rocket engine uses its propellant to produce thrust. Hence, the ideal rocket equation can be written in a more realistic form by using the specific impulse and accounting for other losses as the following:

$$\Delta v = \left(I_{\mathrm{sp}} \ln \frac{m_{\mathrm{i}}}{m_{\mathrm{f}}}\right) - \Delta v_{\mathrm{grav}} - \Delta v_{\mathrm{drag}}\,. \tag{2.6}$$

Now that we have established the necessary parameters and how they are relevant to the ideal rocket equation, it is time to look at the significance of the ideal rocket equation. The inference from Equation (2.1) is that manipulating any two variables makes the third variable become a fixed parameter for mission design. Let us choose to fix one parameter, exhaust velocity, and observe the advantages of a high exhaust velocity. There are three possibilities: 1) keeping the mass of the propellant constant will result in a longer lifetime; 2) for a fixed lifetime, the propellant usage would be reduced, resulting in room/mass for more payload; and 3) for a constant lifetime and fixed propellant and payload mass, the dimensions of the structure can be minimized.

2.2 Classification of Rocket Propulsion

Rocket propulsion can be classified based on many considerations: type of energy source, basic functions, size, type of propellant, and so on. One beneficial way of looking at it is based on the method used to produce thrust. This brings up three main classifications: chemical, electrical, and thermal rocket engines. Comparison[22,23] between different types of thrusters are shown in Table 2-1.

Table 2-1. Thrust-to-Weight Ratio and Specific Impulse Comparison

Type of Propulsion		Thrust-to-weight ratio	Specific Impulse (s)
Chemical	Liquid monopropellant	10^{-1}–10^{-2}	150–225
	Liquid bipropellant	10^{-2}–100	300–450
	Solid propellant	10^{-2}–100	210–320
Electrical	Electrothermal thruster	10^{-4}–10^{-2}	120–300
	Electrostatic thruster	10^{-6}–10^{-4}	1200–3500
	Electromagnetic thruster (pulsed inductive)	10^{-4}	2200

2.2.1 Chemical Rocket Propulsion

Chemical propulsion is the most commonly used form of rocket propulsion. Chemical rockets can provide very high level of thrust, thereby making them the ideal choice for gaining access to space. Chemical rockets carry their own fuel and oxidizer and have internal combustion that can occur in the vacuum of space. Thrust is produced by the effect of chemical reactions that takes place between the fuel and oxidizer. This chemical reaction produces extremely high heat, and the reaction product is then made to expand through a nozzle to increase the exhaust velocity, thereby converting the thermal energy from the chemical reactions into kinetic energy. Chemical rockets are further classified into three common types: solid, liquid, and hybrid rockets.

Table 2-2. Common Types of Chemical Rockets

Type of Chemical Rocket		Characteristics	Reignition
Solid Rockets		Propellant and oxidizer are a solid mixture grain	Cannot stop the combustion and reignite.
Liquid Rockets	Monopropellant	Liquid propellant such as hydrazine, exothermally decomposes as it flows through a catalyst.	Can stop the combustion and be reignited
	Bipropellant	Two liquid propellants are stored separately, mixed in the combustion chamber.	
Hybrid Rockets		Separate stored oxidizer and fuel. Typically, a solid fuel with a liquid oxidizer stored in a tank.	Can stop the combustion and be reignited

2.2.2 Electric Propulsion

Electric Propulsion (EP) is any type of technology in which the exhaust velocity of the propellant is increased using electrical means. EP technology is notable for achieving thrust by accelerating the propellant to reach very high exhaust velocities. If we look at this in terms of the ideal rocket equation, increase in the exhaust velocity could lead to reduction in the amount of propellant used for a mission. However, electric rockets are limited by the amount of available power. Present day technology allows only certain power sources to be carried on-board a spacecraft; this coupled with the power derived from the Sun through solar panels is still a limited source. Despite the power restrictions and lower thrust levels, EP thrusters can reach very high specific impulse compared to other types of rocket propulsion, enabling several space missions: orbit control, space maneuvering, and interplanetary missions. Overall, the future of space propulsion looks to EP thrusters to provide a solution for the in-space propulsion necessity that cannot be provided in a cost-effective manner by the current chemical propulsion devices. There are three main types of EP acceleration: electrostatic, electrothermal, and electromagnetic.

2.2.2.1 Electrostatic Acceleration

Electrostatic thrusters accelerate an ionized propellant by applying direct electric body forces. This circumvents the thermal limitations[20] that limit the achievable exhaust velocity and thrust in a chemical thruster. Thrust is typically achieved by accelerating the ions by creating a potential difference between the source and a negative grid. More recent technologies have used the difference in potential between two gridded plates to accelerate the ions. The thrust achieved by this method depends on three main factors: mass of the ions, exhaust velocity of the ions, total ion flux effectively passing through the grids.

2.2.2.2 Electrothermal Acceleration

Electrothermal thrusters are like chemical thrusters due to the manner in which they generate thrust by expanding hot gas through a nozzle. However, rather than by chemical means, the propellant is heated using electromagnetic energy. Some of the common methods of heating

the propellant are to use arc discharges and high-frequency radiowave excitation. The main drawback of these type of thruster is the capability of their chamber and nozzle to withstand extreme heat; which restricts the thruster from reaching higher values of exhaust velocity.

2.2.2.3 Electromagnetic Acceleration

Electromagnetic thrusters accelerate a stream of ionized gas in a well-established magnetic field by driving current through the propellant stream. In this case, the magnetic field is used to directly accelerate the propellant. Despite several hindrances in the maturing of this technology, electromagnetic thrusters promise high exhaust velocity with high propellant mass flow rate. Hence, electromagnetic thrusters could potentially be serious contenders for future space propulsion if sufficient funding is provided for their research and development.

2.3 Ion Thruster Physics

The ion thruster is a type of electrostatic thruster that uses the acceleration of ions from a plasma source to produce thrust. This is done by generating a potential difference between a set of extraction grids. A neutralizing device is used to recombine the ions and with electrons in the plume, which neutralizes the beam and avoids beam stalling. A classic sketch of the essential elements of an ion thruster is seen in Figure 2-2.

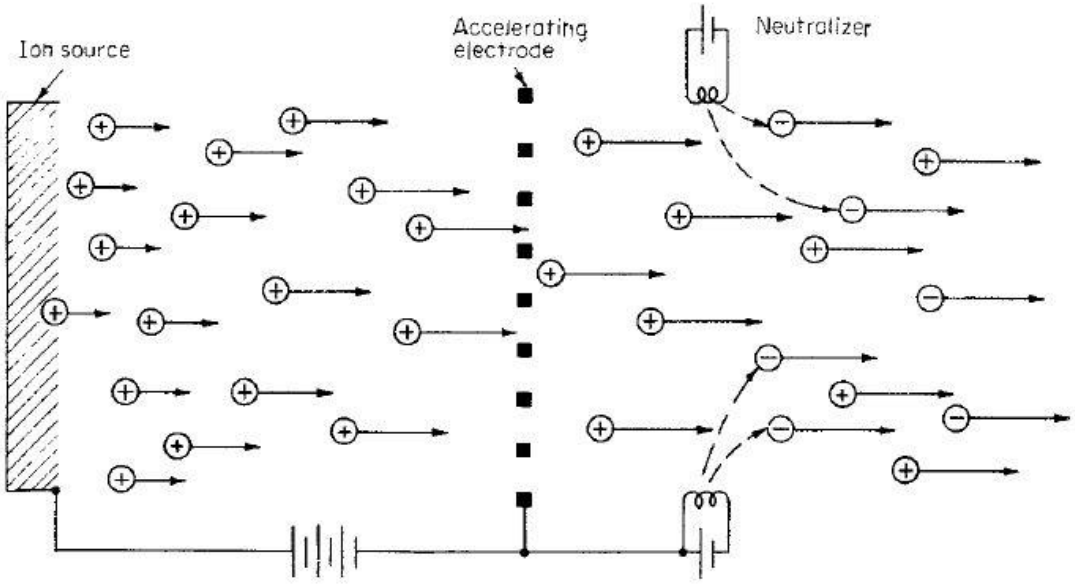

Figure 2-2. Schematic of an ion thruster[20]

2.3.1 Plasma Generation

Ionization of gases can be achieved in several ways, each of which have their own benefits and uses. There are three main plasma generators for ionization: direct current (DC) electron discharges, radio frequency (RF) discharges, and microwave frequency discharges. The subsections below will provide examples of these types of ion thrusters.

2.3.1.1 Bombardment Ionization

Bombardment ionization is the traditional method of plasma generation, which utilizes a thermionic hollow cathode and DC supply to bombard propellant gas with high energy electrons. The schematic shown in Figure 2-3 shows such a system, which was originally designed for using mercury as propellant. However due to several environmental concerns, argon and xenon became the prime candidates for use as propellants. The motion of electrons from the cathode to the anode, which is the ionization chamber wall, causes the electrons to collide with the incoming propellant. A successful collision results in ionization by dislodging electrons from the neutral incoming gas and thereby creating ions.

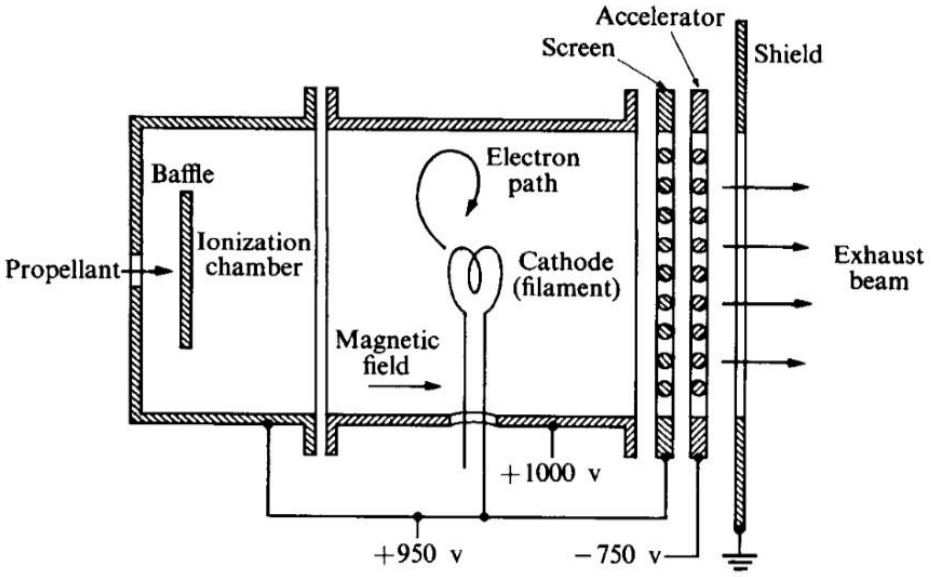

Figure 2-3. Schematic of Kaufman's thruster with typical operating voltages[24]

2.3.1.2 RF Ionization

Radio Frequency (RF) ionization is an inductive method of plasma generation that utilizes electromagnetic fields to heat electrons present in the propellant, which further ionizes the incoming propellant gas. Figure 2-4 represents the schematic of the RIT-XT[25,26] designed by Leiter, which is the traditional design of an RF thruster. The coils are connected to a power supply that provides the necessary RF power needed to generate the plasma. The earlier designs of the RF thrusters did not incorporate an applied magnetic field. However, it is crucial in improving the efficiency and discharge parameters of the system. The typical working frequency used is in the range of 1 MHz.

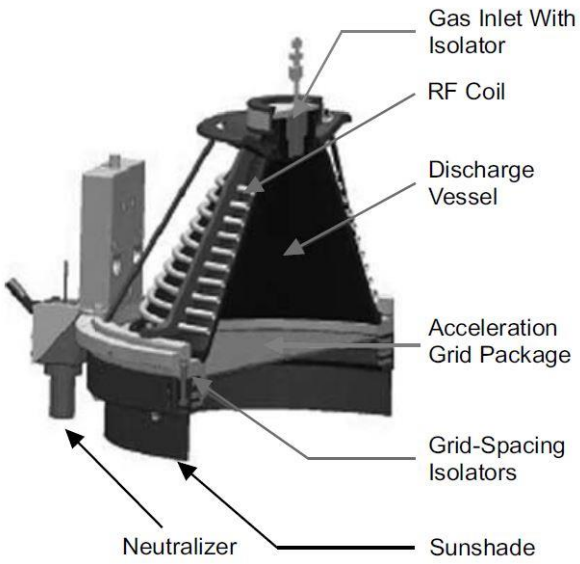

Figure 2-4. Schematic of a RF thruster[26]

2.3.1.3 Microwave Discharge Ionization

Microwave discharge ionization is another method of producing plasma by utilizing electromagnetic fields at microwave frequencies. The DC ionization presents issues with the life of the cathode, limitations of applied DC voltage, and the exposure of cathodes to plasma sputtering. These issues are eliminated in inductive plasma generation. However, the frequency of the plasma and the plasma density play an important role in the efficiency of the system. If the frequency is too high or the plasma density is too low, then the microwave power supplied will be reflected to the source. This raises concerns and establishes the need for optimization of the microwave system especially when miniaturizing the technology.

2.3.2 Electron Cyclotron Resonance in MMIT

Miniaturization of ion thrusters is challenging due to the conditions required for plasma generation and extraction at a reduced scale. The MMIT[6] works by generating an electron cyclotron resonance (ECR) discharge plasma using microwave power transmitted via an antenna and a strong magnetic field to confine the electrons. The electrons acquire energy through the ECR process and

start to collide, and as a result create additional ions and electrons. This process depends on the electromagnetic interaction established by the microwave antenna and the strong magnetic field, which is based on the dimensions and positions of the components. The ions thus generated are then extracted through electrostatic grids, thereby generating thrust in the system.[27,28]

2.3.3 Neutralization

Beam stalling is an issue when dealing with the emission of charged particles. The ion thruster expels ions, which are positively charged, by accelerating them through the extraction grids. The expelled positive ions will charge the neutral space environment and give it an overall positive charge. At the same time, the spacecraft itself acquires a negative potential from the loss of the ions. This change in dynamics between the spacecraft and the space environment results in the ions being attracted back into the system to maintain net neutral charge. The neutralizer is used to avoid this effect by emitting electrons to recombine with the ions expelled by the thruster as depicted in Figure 2-2. Typical neutralizers are electron guns and thermionic emitters.[29]

2.4 Thrust Parameter Calculations

This section provides the equations used to calculate thruster parameters using experimental data, which include thrust, specific impulse, and efficiencies. Exhaust velocity (u_{e}) depends on the charge-to-mass ratio across a given potential difference, and can be written as[20]

$$u_{\mathrm{e}} = \sqrt{\frac{2q\mathrm{V}}{m}}, \tag{2.7}$$

where m is atomic mass of the propellant, which in this work is argon. Specific impulse (I_{sp}) can be calculated from[19]

$$I_{\mathrm{sp}} = \frac{1}{g_{\mathrm{e}}}\sqrt{\frac{2qV}{m}}, \tag{2.8}$$

or

$$I_{\mathrm{sp}} = \frac{1}{g_{\mathrm{e}}}\frac{\tau}{\dot{m}_{\mathrm{p}}}. \tag{2.9}$$

Ideally, if the beam can completely pass through the acceleration grids, the thrust per unit area is given by[19]

$$\frac{\tau}{A} = \frac{8}{9}\varepsilon_0 \left(\frac{V}{L}\right)^2 \tag{2.10}$$

Thus, maximum thrust is based on the potential difference between the two acceleration grids, i.e., the acceleration electric field, which must be below the voltage-breakdown limit between the two grids.

In electric propulsion, the thruster has highly efficient utilization of propellant mass, which can be defined as mass utilization efficiency, η_M, which accounts for ionized versus un-ionized propellant and is defined for singly-charged ions as[22]

$$\eta_{\mathrm{M}} = \frac{I_{\mathrm{b}}}{q}\frac{m}{\dot{m}_{\mathrm{p}}}\,. \tag{2.11}$$

The total efficiency, η_T, is defined as the jet power divided by the total electrical power into the thruster, i.e.,

$$\eta_{\mathrm{T}} = \frac{P_{\mathrm{jet}}}{P_{\mathrm{in}}}\,. \tag{2.12}$$

The jet power of any electric propulsion thruster can be written as

$$P_{\mathrm{jet}} = \frac{\tau^2}{2\dot{m}_{\mathrm{p}}}\,. \tag{2.13}$$

Thus, the total efficiency can be expressed as

$$\eta_{\mathrm{T}} = \frac{P_{\mathrm{jet}}}{P_{\mathrm{in}}} = \frac{\tau^2}{2\dot{m}_{\mathrm{p}}P_{\mathrm{in}}}\,. \tag{2.14}$$

Chapter 3

MMIT Design

The MMIT design has undergone multiple iterations to reach the current version shown in Figure 3-1. Here, we outline the design considerations and revisions made to previous designs. The original version[12] was designed to operate at 4.2 GHz, but was later shown that this was not the appropriate operating frequency for the thruster, which explained its performance issues. Taunay's[15] redesigned version of the MMIT (inspired by JAXA's μ1 thruster design[8]) incorporated elements of the original thruster design while changing its operating frequency to 4.9 GHz. However, there remained some mismatches, which limited microwave power absorption, along with arcing problems between the grids and between the grids and the microwave antenna.[15] These problems were mitigated by applying minor changes in the system and characterizing the system. This chapter presents the walkthrough of the design carried over from Taunay's redesigned version of the thruster along with an overview of the MMIT design considerations.

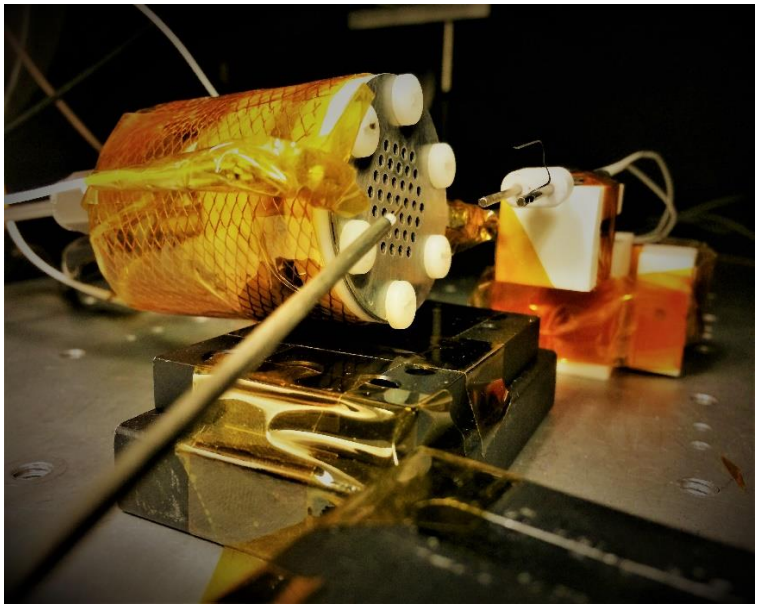

Figure 3-1. Latest MMIT version

3.1 Design Overview

The prototype described here is fabricated with materials that are different from those of a flight thruster to facilitate an iterative design process and to reduce costs. These materials are the same as the previous test version of the MMIT. With reference to Figure 3-2, the back plate is made of Macor®, as it is a carbide-machinable ceramic. The yoke plate is made of a low-carbon steel alloy (Steel 1018) with a high relative magnetic permeability, required to complete the magnetic circuit. The magnets are made of neodymium (Nd–Fe–B) and placed as two concentric circular magnets with the ring antenna located at the center of the magnets. The microwave input power is provided by an SMA candlestick that is shielded by a stainless-steel tube to reduce the power reflections in the microwave line. This line is attached to the antenna, which is made of copper. The gas enters the discharge chamber through 8 holes placed on the yoke plate such that the gas flows in between the two concentric magnets. The discharge chamber is 22.33 mm in diameter and leads towards the Macor front plate.[15,16] The extraction grids are made of stainless steel, with a polytetrafluorethylene (PTFE) spacer between them. There are 37 holes in a hexagonal grid with an aperture diameter of 1.613 mm for the screen grid, 1.321 mm for the acceleration grid. The thickness of the screen and acceleration grids is 0.635 mm, and the spacer in between the grids is 0.508 mm. The Faraday cage around the thruster is made of a copper mesh with a layer of Kapton® film to prevent it from arcing.

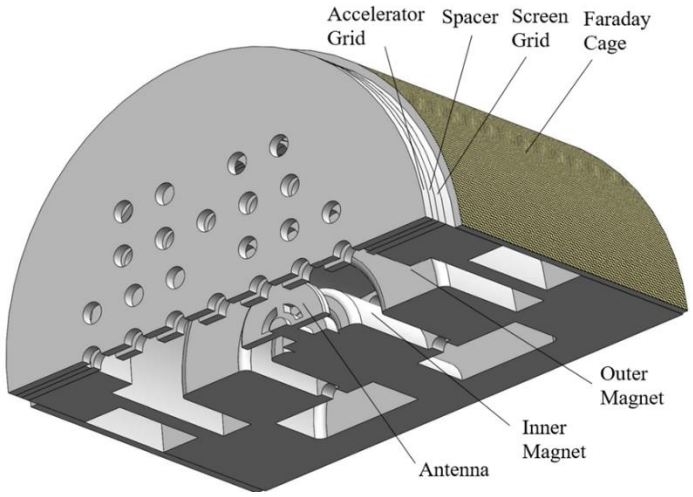

Figure 3-2. Cross-section view of current MMIT version

3.2 Back Plate

The back plate is part of the modular design of the MMIT; it is fastened to the front plate and houses the yoke plate inside it. The back plate also accommodates the propellant feed and microwave input as seen in Figure 3-3, which are essential for the operation of the thruster. Proper sealing is ensured by the addition of the vacuum sealant used to secure the possible leaks in the system.

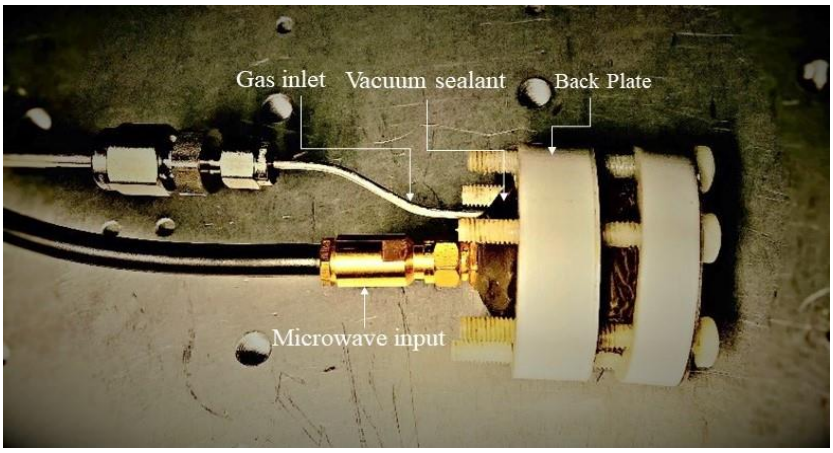

Figure 3-3. Top view of the MMIT

3.3 Yoke Plate

The yoke plate (Figure 3-4) has two main purposes: to transition the propellant from the expansion chamber to the discharge chamber and to hold the concentric magnets that complete the magnetic circuit. The magnets are placed with their poles inverted relative to each other in order to create a magnetic bottle between them for the completion of the magnetic circuit. This naturally requires the yoke plate to be made of a material with high relative magnetic permeability, typically, low-carbon steel or iron. Table 3-1 shows the properties[30–33] of the different types of magnets that were considered for the MMIT design.

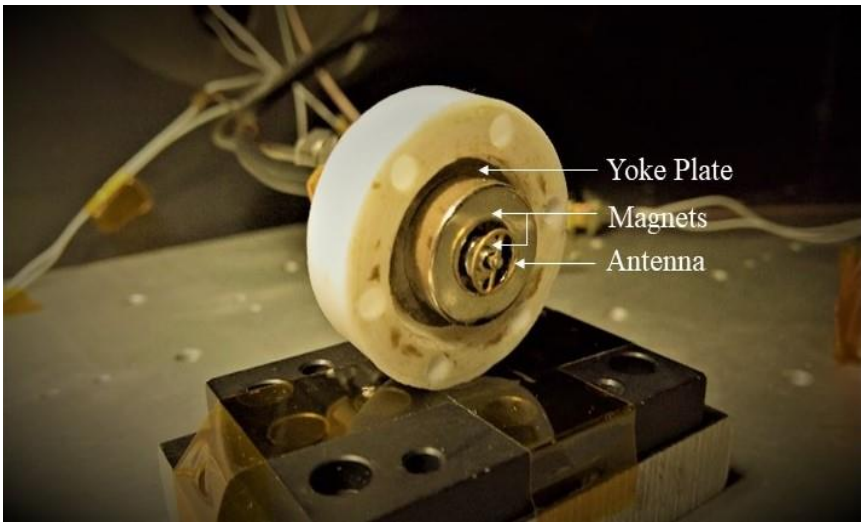

Figure 3-4. Yoke plate with magnets and antenna

Table 3-1. Properties of Magnets Considered for the MMIT

Magnet Type	**Maximum Operating Temperature (°C)**	**Curie Temperature (°C)**
Neodymium (grade N42)	80	310
Samarium–Cobalt (2-17 alloy)	300	800
AlNiCo	400–500	815–890

Magnet Type	**Residual Flux Density, B_r (T)**	**Temperature Coefficient, T_c (%/K)**
Neodymium (grade N42)	1.3	−0.13
Samarium–Cobalt (2-17 alloy)	1.2	−0.035
AlNiCo	1.0	−0.2

3.3.1 Expansion Chamber

The space between the magnets is utilized by placing eight holes of 1 mm diameter to serve as the input of propellant from the expansion chamber to the discharge chamber. The expansion chamber is the space between the inner wall of the back plate and the back plate.

3.3.2 Candlestick Antenna

The microwave candlestick is introduced into the chamber through a central hole in the yoke plate that was designed based on the dimensions of the inner magnet and would need to be changed if the dimensions[34–36] of the inner magnet are altered. Table 3-2 shows the difference in the dimensions of the magnets between the original version and the current version of the MMIT. The current version is the same as the previous design. The only changes made were during the experimental procedures in terms of realignment of the magnets and the antenna according to the theoretical prediction.

Table 3-2. Dimensions of the Magnets

Magnet	**Dimension**		**Current Version** (inches)	**Original Version** (inches)
Inner Magnet	Diameter	Inner	1⁄8	1⁄16
		Outer	1⁄4	1⁄8
	Thickness		1⁄4	—
Outer Magnet	Diameter	Inner	3⁄8	1⁄4
		Outer	3⁄4	3⁄8
	Thickness		1⁄4	—

3.4 Flight Version of MMIT

A flight version of the MMIT would use xenon as propellant, which is easier to ionize and has a higher atomic mass than argon. The yoke plate would be made of iron and the permanent magnets would be made of samarium–cobalt (Sm–Co), which has a higher Curie temperature of 800 °C, necessary as the MMIT heats up during operation. The Faraday cage is being redesigned to fit around the discharge chamber using an aluminum mesh. The glass quartz[15] discharge chamber has the benefit of being able to observe the plasma formation in the thruster during testing, but would not be used for a flight version; rather, ceramic would be used. The extraction grids would be made of molybdenum for its low sputter erosion rate, good thermal and structural properties, and its ability to be chemically etched to form the aperture array. Hence, the grids would be manufactured with a chemical etching process that would provide tighter tolerances and eliminate sharp edges where arcing could occur.[37]

Chapter 4

Experimental Setup

Testing of the current MMIT prototype and its predecessor designs was conducted within a thermal–vacuum chamber at Penn State that is used for testing our propulsive devices and other projects under a simulated space environment. This chapter provides an overview of the experimental setup and the equipment used in the current iteration of the experimental research conducted on the MMIT.

4.1 Vacuum Chamber

The vacuum chamber has a diameter of approximately 0.6 m and depth of 1.0 m. The vacuum flanges accommodate the necessary feed-through connections and other connectors to facilitate the interaction with the external device necessary to operate the thruster. The vacuum chamber has a dual-pump setup that uses a dry pump and a cryo-pump to reach high vacuum conditions. Figure 4-1 shows the vacuum chamber used for testing the MMIT.

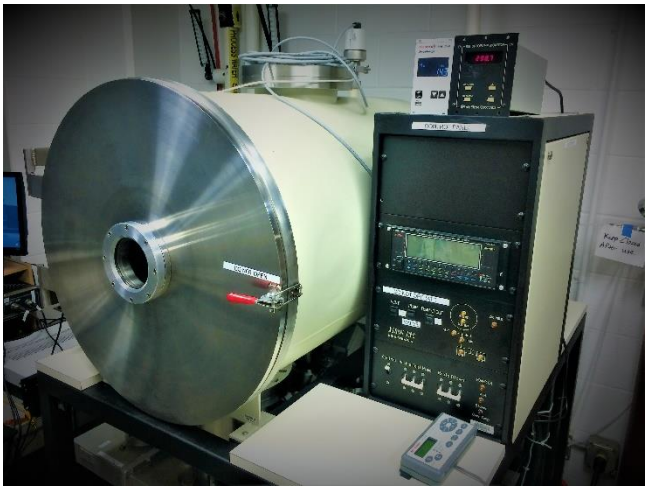

Figure 4-1. Thermal–vacuum chamber

4.1.1 Dry Pump

A BOC Edwards IPUP dry pump is used to pump the chamber down to a pressure of approximately 4×10^{-3} Torr. The pump is equipped with its own thermal sensor to monitor the operational temperature. It is important not allow the temperature to reach above 80 °C to ensure the optimal operation of the pump. This pump is suction based and has relevant valves added to the vacuum chamber system to allow for re-pressurization without any back suction. This is essential in preventing foreign particles from affecting the experimental procedure.

4.1.2 Cryo-Pump

High vacuum conditions are reached by using a CTI-Cryogenics Cryo-Torr 10 series cryopump, which brings the chamber down to a base pressure of approximately 1×10^{-5} Torr. The principle of operation is that gases can be condensed and held at extremely low vapor pressure.[38] The cryopump head temperature is ideally brought down to about 25 K before the gate valve is opened. The temperature of the head is monitored with a Lakeshore Cryotronics, Inc. 818 cryopump monitor.

4.1.3 Pressure Sensor

The pressure inside the vacuum chamber is monitored by a Pfeiffer Vacuum Inc. PKR 251 Compact Full Range Gauge, which has a range of 7.5×10^{2} to 3.75×10^{-9} Torr. This is coupled with a Pfeiffer Vacuum Inc. single gauge pressure sensor.

4.2 Microwave Power System

With reference to Figure 4-2, the microwave signal required to create the plasma in the MMIT is generated by a Hewlett-Packard 8683D Signal Generator, which has a frequency range of 2.3–13.0 GHz. This signal is amplified using a Hughes 8010H Traveling Wave Tube Amplifier,

which has a frequency range of 4.0 GHz to 8.0 GHz with 30-dB power gain. Figure 4-3 shows the equipment used during for conducting the experiments.

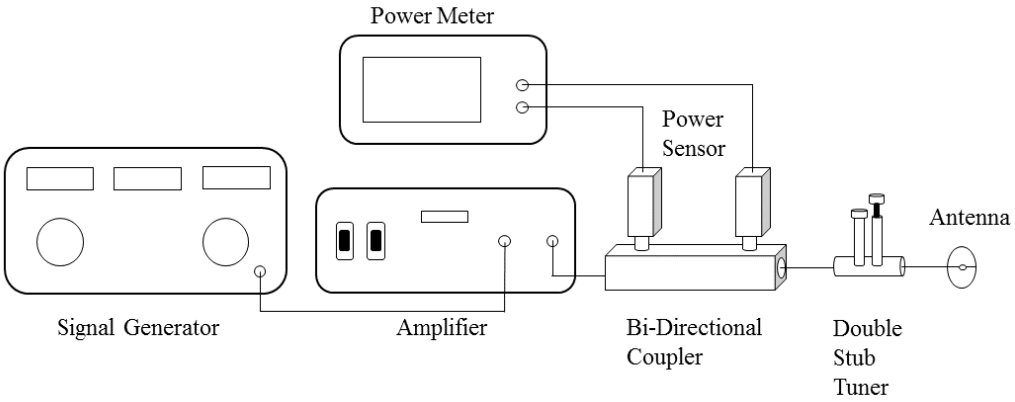

Figure 4-2. Schematic for microwave power injection into MMIT

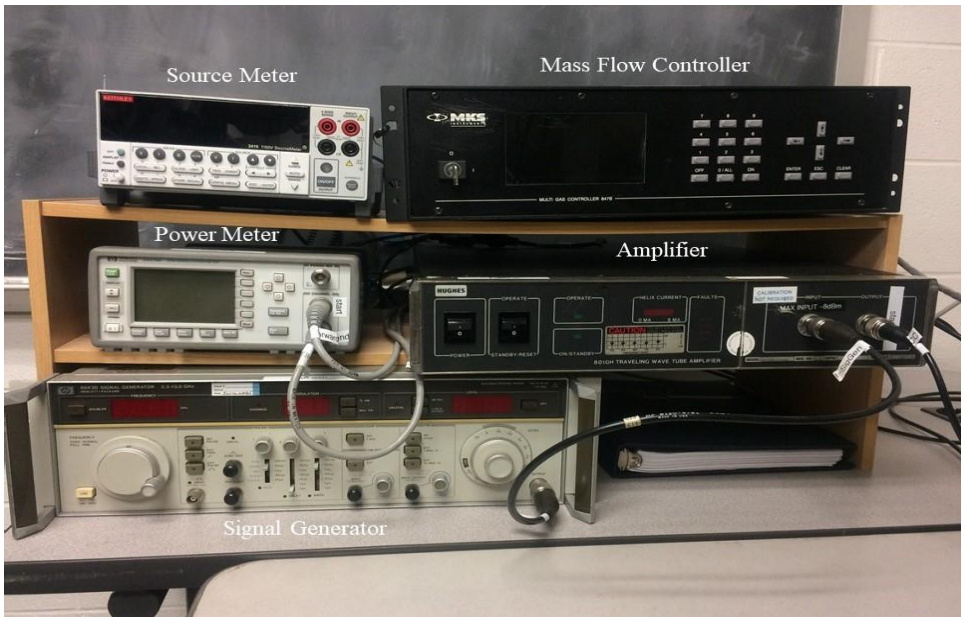

Figure 4-3. Equipment used to generate microwave power

4.2.1 Bi-directional Coupler, Power Meter, and Double-Stub Tuner

A Narda 3024 bi-directional coaxial coupler is used to measure the forward and reflected power of the system with two Agilent power sensors[39] that operate in the range of 10 MHz to 18 GHz, connected to a Hewlett-Packard E4419A EPM series[40] power meter as shown in Figure 4-4. Impedance matching between the microwave coaxial feed line and the thruster's input antenna is achieved using a Harris 306A double-stub tuner. These components are connected in series with coaxial cables and the final output is sent inside the chamber through an SMA feed-through.

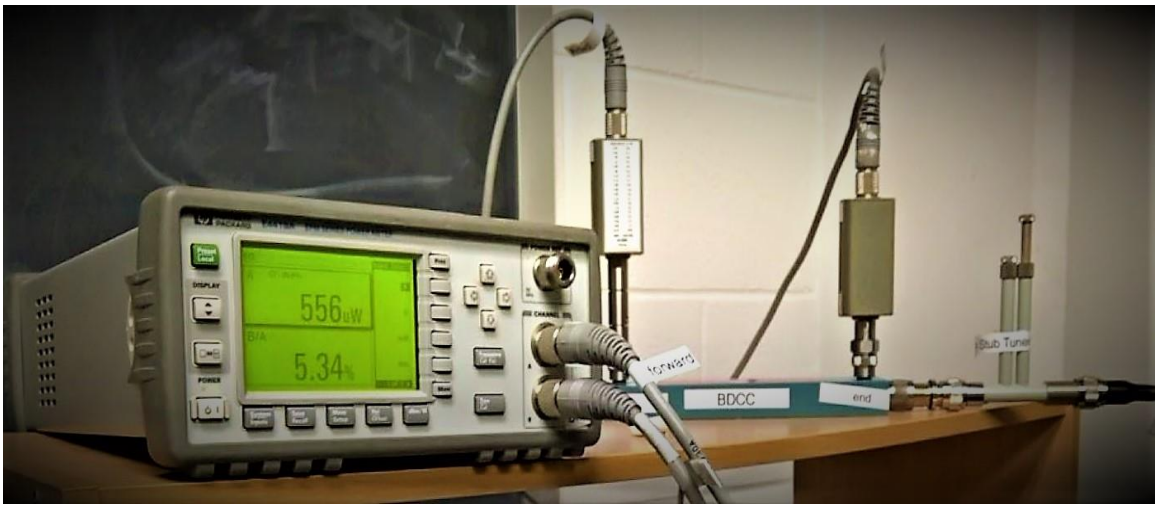

Figure 4-4. Bi-directional coupler, power meter, and double-stub tuner

4.3 Extraction Grid System

The extraction grid voltages are set using a Stanford Research Systems, Inc. Model PS310 high-voltage power supply[41] with a maximum DC voltage of 1250 V and a Stanford Research Systems, Inc. Model PS350 with a maximum voltage of 5000 V. The high-voltage power supplies are connected using BNC coaxial cables. Additionally, an Oriel 70705 high-voltage power supply,[42] with a max DC voltage rating of 2000 V, is used to run arc test on the grids. This is done to bypass the auto reset properties of the Stanford equipment, thereby allowing us to conduct various experimental procedures and record the setup under test.

4.4 Propellant System

A flight version of the MMIT would use xenon as propellant, which has a lower ionization energy of 12.1 eV and a higher atomic mass than argon. However, the experimental procedures are performed with argon as propellant since the overall cost of using xenon is much higher. A stainless-steel pipe 1⁄8 inch in diameter and a CF gas feed-through line is used to supply the discharge chamber with a 99.999% purity argon. A MKS Multi Gas Controller 647B coupled with a MKS ALTA Digital Mass Flow Controller 1480A,[43] capable of operating at low mass flow ranges (<10 sccm), was used to control the mass flow of argon to the thruster. The interface consists of a Swagelok fitting leading into the 1⁄16 inch in diameter inlet pipe on the thruster.

4.5 Measurement Methods

A Keithley 2410 source meter is used with the Langmuir probe and Faraday cup for measuring ion beam currents (Figure 4-5). The Langmuir probe is used to measure the ion density, ion temperature, and the ion beam current. The Faraday cup is used to measure the current density of the beam. Data from both these devices are used to calculate thrust.[44]

The Langmuir probe is placed in the path of the extracted ion beam to acquire meaningful results. It is placed a few centimeters away from the acceleration grids in order to prevent arcing between the probe and the extraction grids. The distance is determined such that the probe is not subjected to interferences from the extraction grids or the microwave discharges. The data gathered from the voltage sweep are processed using a LabVIEW program to extract the plasma parameters.

The Faraday Cup is placed approximately the same distance away as the Langmuir probe. However, its position is radially varied in increments of 5° to effectively characterize the dispersion of the ion beam.

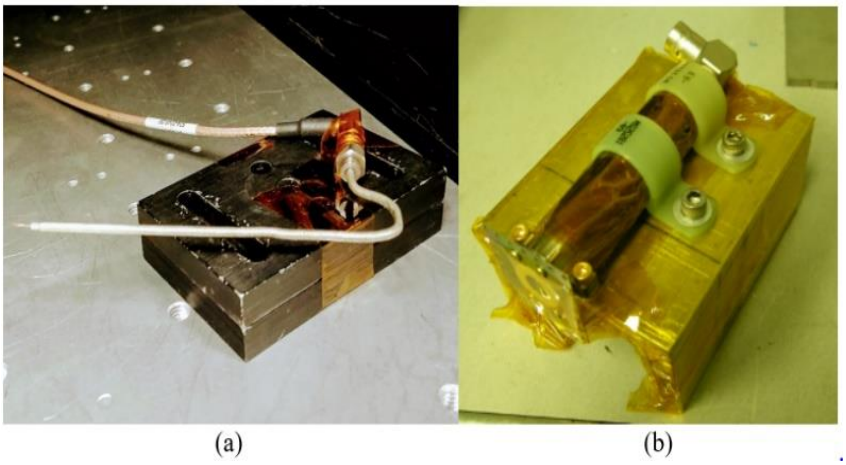

Figure 4-5. (a) Langmuir probe and (b) Faraday cup

4.6 Microwave Analysis

An Agilent Technologies ENA Series E5071C Vector Network Analyzer (VNA) with a range of 9 kHz–8.5 GHz was used to perform the microwave analysis[45–47] of the thruster and the microwave input line to generate a log-mag plots of the reflected power (S_{11}) over the operating frequency range. This was essential in determining the ECR frequency of the thruster to successfully lower the input power required during ionization. The network analyzer also provides significant information to match the impedance (50 Ω) of the microwave source and the thruster to reduce reflected power. The use of the double-stub tuner coupled with the VNA has been crucial in the lowered power requirements achieved with this MMIT iteration.

Chapter 5

Results

Our research thrusts for the current MMIT iteration have been the following: demonstrating plasma generation; sustaining and containing the plasma; and extracting the ion beam. The work done on the MMIT has been iterative between experimental and numerical simulations. Each iteration brings us closer to the desired end goal of the MMIT project, which is to have a fully functioning flight thruster suitable for applications on micro-spacecraft, such as CubeSats.

5.1 Previous Results and Overview

The previous MMIT iteration could create plasma only at higher power levels than what numerical simulations had predicted and was unsuccessful in extracting the ion beam. Since the MMIT project is an iterative process and there has been a considerable time gap in the research, there is a necessity to validate certain steps performed in the previous iteration to understand the differences that exist between the numerical and experimental results. Therefore, along with testing the previous setup of the thruster, the numerical simulations were also performed as a form of validation.

This chapter presents the numerical simulations performed as part of the validation process by introducing minor changes made in the system into the previous numerical model. However, the specific goals for this iteration were to lower the overall power requirements, reduce microwave power reflected by the thruster head, and demonstrate extraction of ion beam. Achieving these goals allows us to calculate thrust, specific impulse, and efficiency based on experimental data rather than numerical simulations.

5.2 Numerical Simulation

Numerical simulations were performed using COMSOL Multiphysics to understand the minor changes made to the previous version of the thruster without going deeper into the realm of ion optics or other particle-in-cell simulations. COMSOL Multiphysics is a multi-purpose software platform that relies on the finite element method (FEM) to solve partial differential equations (PDEs) for its modeling[48–50] and simulations of physics-based problems. COMSOL Multiphysics allows you to account for coupled, or "multiphysics", phenomena. Furthermore, modularity of the software helps it to evolve in ways to keep up with recent updates in many fields. The software's modules make it relatively easy to apply strict requirements that mirror the experimental results with a relatively high level of confidence. COMSOL Multiphysics was used in this work to determine the effective ECR region within the thruster by simulating the electromagnetics of the thruster geometry. This is crucial in establishing the position and orientation of the antenna in the thruster.

5.2.1 Magnetic Field

The magnetic field generated by the two concentric magnets used in the MMIT were simulated in COMSOL Multiphysics to illustrate the position and range of the effective ECR region. This is a crucial step to determining the relative position and orientation of the antenna. The magnetic fields (no current) module under the AC/DC physics interferences is used in this case to compute the stationary magnetic field generated by the permanent magnets. In this section, we only determine the ECR zone with the magnetic field. Therefore, only the magnets and the yoke plates were simulated while ignoring all other parts of the thruster.

5.2.1.1 Geometry

Permanent magnets are ideally simulated in 3D space. However, the geometry is analyzed in a 2D symmetric plane to simplify the simulation of the thruster without compromising results, which is possible since the thruster is axially symmetric; the geometry is further simplified by only projecting half the cross section.

As discussed in Chapter 3, the geometry of the magnets is concentric in nature and have their poles inverted with respect to each other. The last part of the design is a yoke plate to connect and effectively close the magnetic circuit between the two concentric magnets as seen in Figure 5-1.

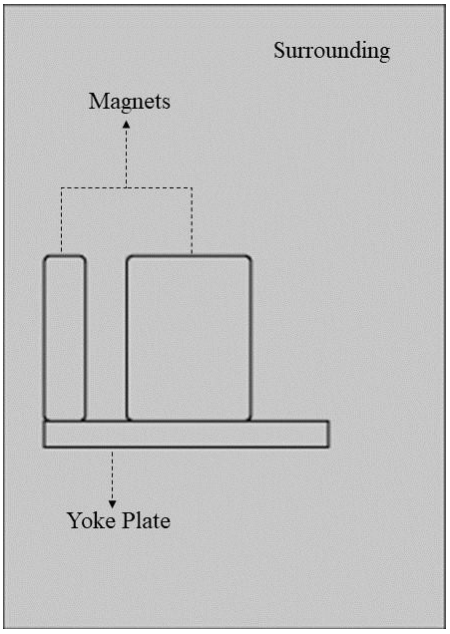

Figure 5-1. Geometry for magnetic field simulation

5.2.1.2 Materials

COMSOL Multiphysics requires the relative magnetic permeability μ_r to simulate the magnetic fields from the given geometry. Table 5-1 provides the relative magnetic permeability for the materials[51–53] used in the MMIT. All the materials for each domain in the overall geometry must be well defined. The material property for samarium–cobalt must be manually added into the system as it does not exist as part of the default module.

Table 5-1. Material and Relative Magnetic Permeability of the Geometry

Geometry	Material	Relative Magnetic Permeability
Surrounding	Air	1
Yoke Plate	Iron	4000
Magnets	Samarium–Cobalt	1.05

5.2.1.3 Boundary Conditions

The boundary conditions should be manually set up to override the preset settings. Since we are dealing with magnets, the magnetic flux density is an important factor that defines our magnet to be a permanent magnet of a desired material. In order to do this, the constitutive relation has to be defined as

$$B = \mu_{\mathrm{r}} H + B_{\mathrm{r}} , \tag{5.1}$$

where the permeability constant is $4\pi \times 10^{-7}$ H·m^{-1}. This value primarily depends on the relative permeability of the material and the B_{r} value for samarium–cobalt is 1.2 T. The remnant flux density is defined as a positive value for the inner magnet to ensure that it would represent the north pole and negative for the outer magnet.

Table 5-2. Remnant Flux of the Magnetic Materials

Material	Remnant Flux Density [T]
Neodymium	1.32
Samarium–Cobalt	1.2

5.2.1.4 Mesh

The final step before COMSOL Multiphysics begins its computation is to create a mesh that best suits our need for precision in the area of interest. This allows the user to refine the domain or boundary on the geometry to avoid jump conditions on sharp edges. In this simulation, physically controlled mesh is chosen since the sharp edges have already been filleted. The accuracy of the result depends greatly on the element size of the mesh selected. An extremely finer mesh has been selected for more accurate results. Figure 5-2 shows the finer messing element for this geometry and Figure 5-3 shows the statistic of the mesh. The average element quality is around 0.98. The quality histogram shows that almost all the elements are high quality.

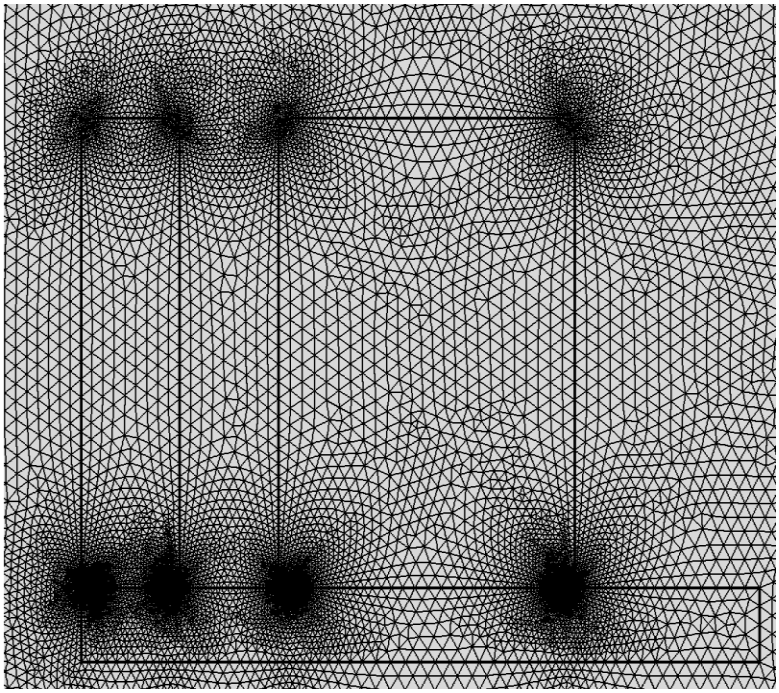

Figure 5-2. Finer meshing of the MMIT geometry

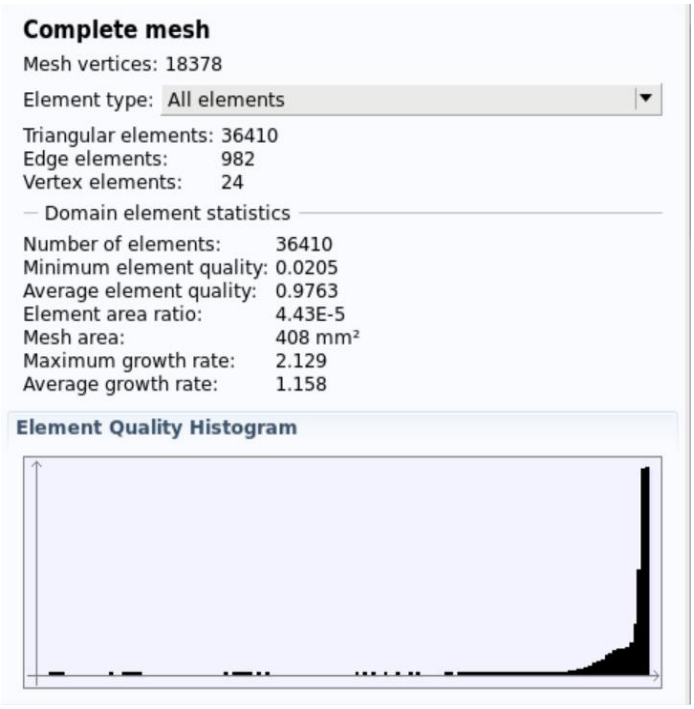

Figure 5-3. Quality of mesh

5.2.1.5 Solver

A solver should be manually selected to override the default method provided for each physics problem in COMSOL Multiphysics. A variant of the GMRES[54] (Generalized Minimal Residual Method) is selected as an iterative preconditioning method. This method uses a Multigrid as the preconditioner and the FGMRES[55] method to solve the problem in this thesis which is a Flexible-GMRES method that allows larger flexibility in the choice of solution subspace than GMRES . Figure 5-4 shows the iteration process running about 130 times before converging.

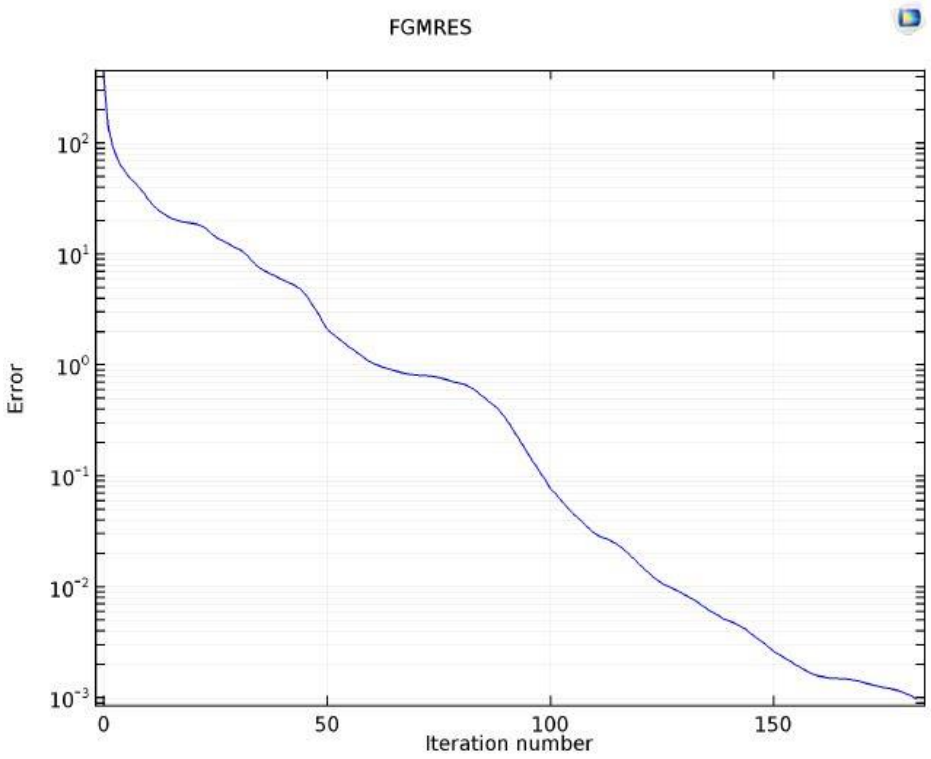

Figure 5-4. FGMRES convergence

5.2.1.6 Results

The number of degrees of freedom are 73,165, and it takes about 4 s to run the simulation. In Figure 5-5, the black line is the magnetic flux density and the color legend is magnetic flux density norm. We find that the magnetic flux density is around 0 to 0.6 T. Therefore, we set the plot to display within this range to show that the field strength is varying outward from the near surface of magnet. We also can see that the streamline of magnetic flux density near symmetrical axis is vertical, this is the region where antenna should be placed to create E ⊥ B.

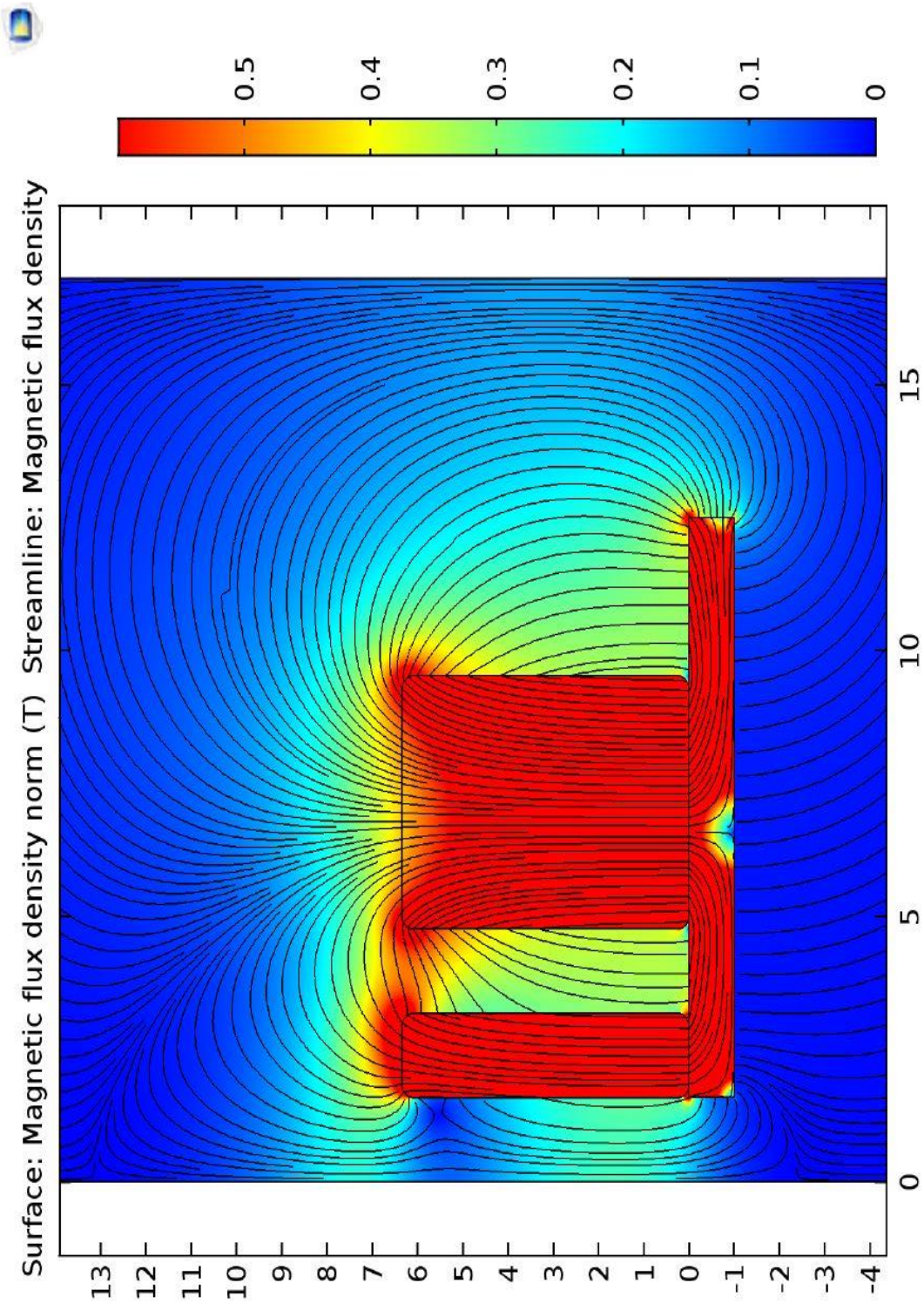

Figure 5-5. Magnetic flux density

The active ECR region is determined from the simulated results. The frequency range corresponding to the location is expected to be around 4 to 5 GHz. We can also determine the electron cyclotron frequency from

$$\omega_c = \frac{qB}{m}, \tag{5.2}$$

or

$$f = \frac{qB}{2\pi m}, \tag{5.3}$$

where q is the elementary charge, and m is the mass of an electron. Therefore, we can obtain

$$f = 28 \times 10^9 \times B, \tag{5.4}$$

where B is the magnetic flux density calculated by COMSOL Multiphysics.

Figure 5-6 shows the frequency range from 4 to 8 GHz corresponding to the distance in the z-direction from the yoke plate. This is critical in determining the position of the antenna and its corresponding distance from the magnet. Since the expected frequency of the active ECR region is around 4 to 5 GHz and the optimal frequency determined experimentally is around 4.98 GHz. Figure 5-6 was used to determine the positions for the antenna in z-direction that falls within the expected frequency range as the following: 0.2 mm, 3.7 mm, 6.5 mm, and 8.3 mm.

Placing the antenna 8.3 mm distance away from the yoke plate, which is 2 mm away from the magnets, seems to be the better solution to maximize the E⊥B interaction for the current design of the thruster. This is chosen after considering the simulated result in Figure 5-7 which shows the location of the active ECR region to stretches between 7 to 9 mm away from the yoke plate

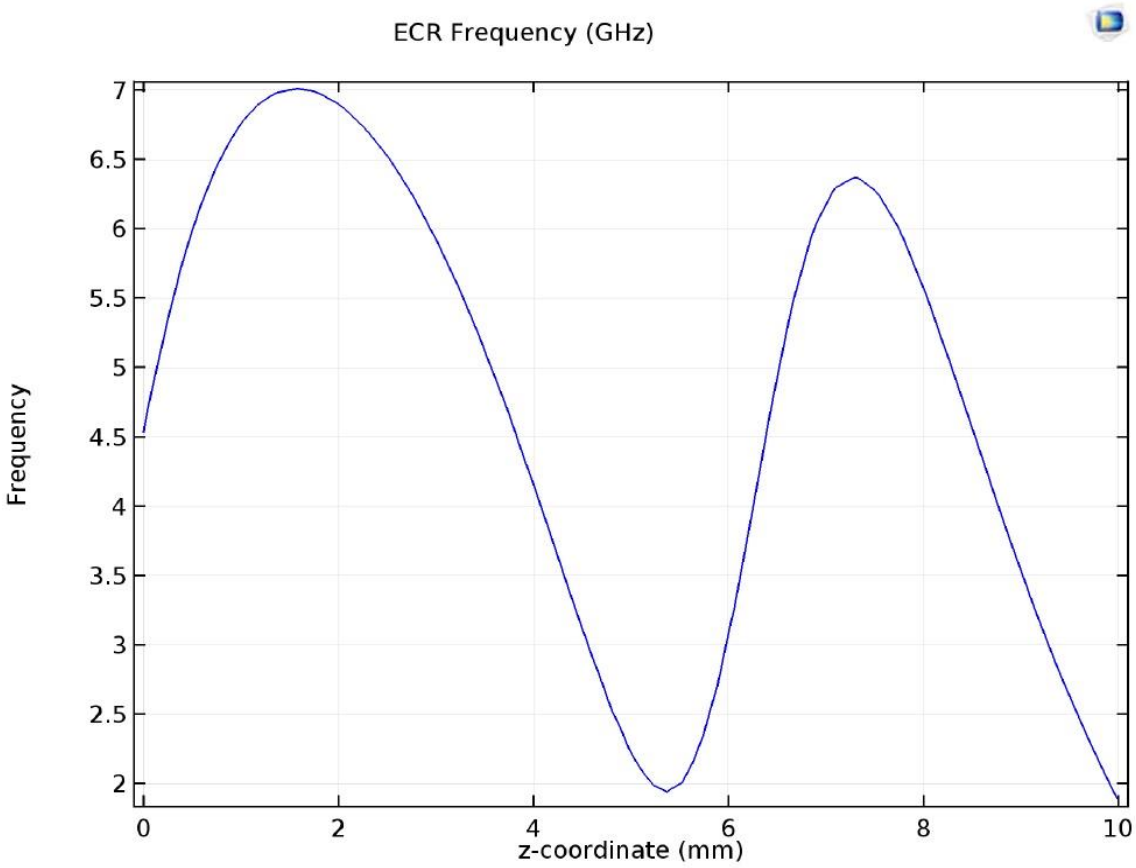

Figure 5-6. ECR frequency range

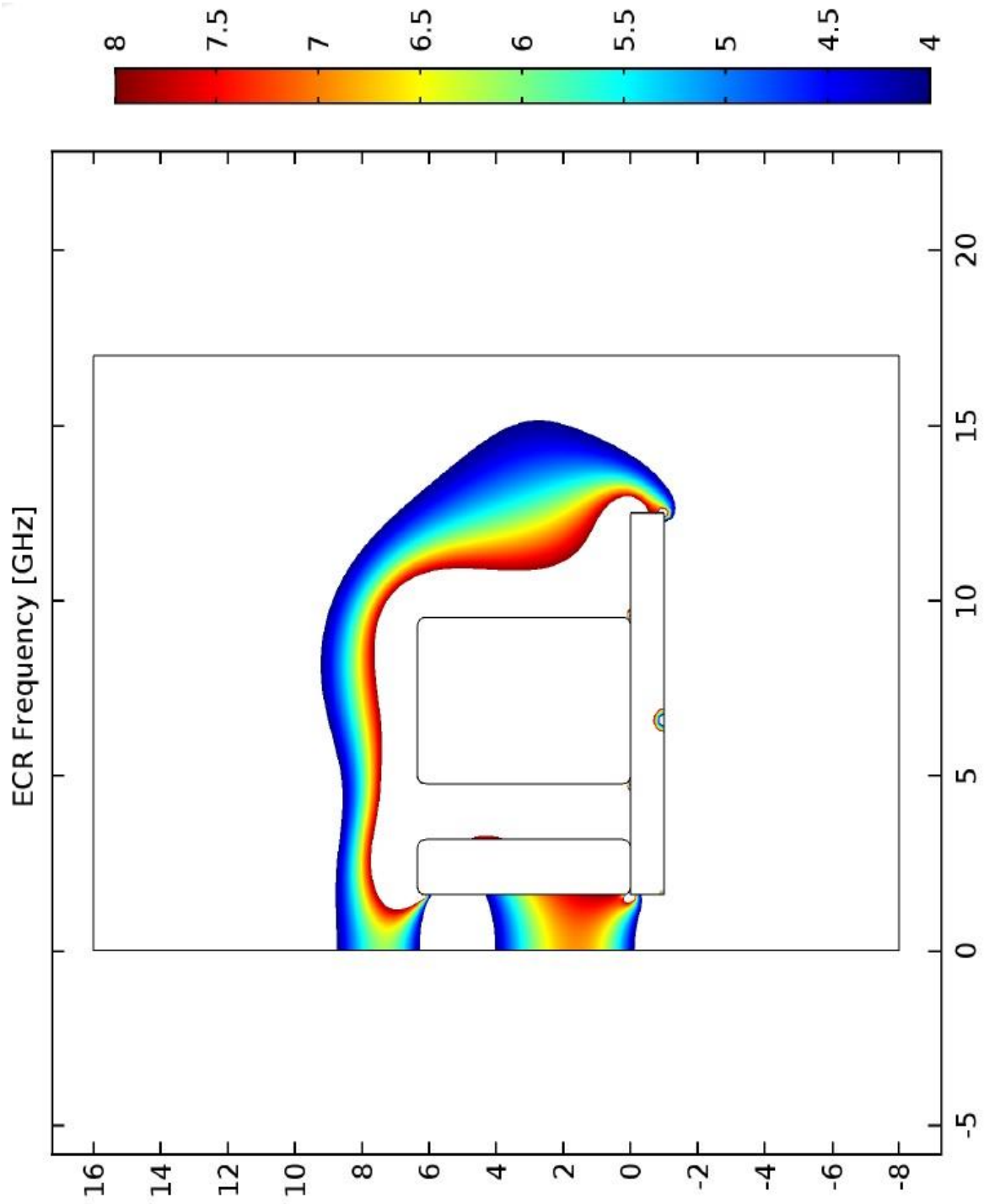

Figure 5-7. ECR region

5.2.2 Ring Antenna Simulation

The electric field generated by the ring antenna used in the latest version of the MMIT was simulated and superimposed with the magnetic field generated by the permanent magnets. This is a crucial step in verifying that the selected position and orientation of the antenna ensures that the E ⊥ B field lines are intersecting at the desired ECR region. Since there is a subtle change in the domain of the geometry in replacing the disk antenna with a ring antenna, the magnetic field simulation is also performed during the antenna simulation. However, most of the parameters are like the previous simulation efforts.

5.2.2.1 Geometry

Defining the geometry for the antenna simulation requires a bit more work compared to the magnetic field. The far-field effects are considered and any component that could cause an interference with the E × B field is considered as part of the geometry for this simulation. Apart from the antenna and magnets; we have the vacuum chamber wall (far field domain), Faraday cage, extraction grids (modeled as simple metal plate), Teflon insulator, and antenna shield (Figure 5-8).

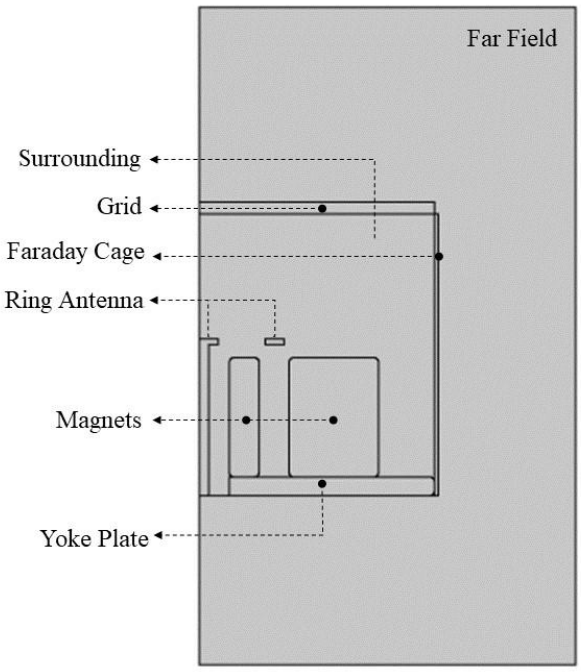

Figure 5-8. Antenna geometry

5.2.2.2 Materials

The same module used for the above simulation is used for the antenna simulation as well. Hence, it is important to define all the materials used in the geometry. Table 5-3 provides the materials used and their relative permeability, relative permittivity, and electrical conductivity. Some of these values are acquired from the online references and manually added into the system to provide COMSOL Multiphysics with the material properties.

Table 5-3. Material and Relative Magnetic Permeability of the Geometry

Geometry	**Material**	**Relative Permeability**	**Relative Permittivity**	**Electrical Conductivity (S/m)**
Far Field Domain	Air	1	1	0
Surrounding	Air	1	1	0
Yoke Plate	Iron	4000	1	1.12×10^{7}
Magnets	Samarium–Cobalt	1.05	1	1.62×10^{7}
Faraday Cage	Copper	1	1	5.998×10^{7}
Antenna	Copper	1	1	5.998×10^{7}
Discharge Chamber	MACOR	1	5.8	0
Insulator	Teflon	1	2.07	0
Grids	Steel	1	1	4.032×10^{6}

5.2.2.3 Boundary Conditions

The boundary conditions chosen are the same from the previous iteration. A *Far Field Domain* condition is selected for the outermost boundary and a scattering boundary condition is used for the cylindrical waves. The bottom part of the Teflon insulator is set as a coaxial port with a wave excitation mimicking the input power of the microwave system.

5.2.2.4 Mesh

The final step before computation begins is to create a mesh that best suits the required level of precision. Unlike the model with just the magnets, the antenna simulation is complex due to the geometry. Finer mesh is selected around the edges, including the connections between different components. Figure 5-9 shows the finer messing element for the antenna geometry and Figure 5-10 shows the statistic of the mesh.

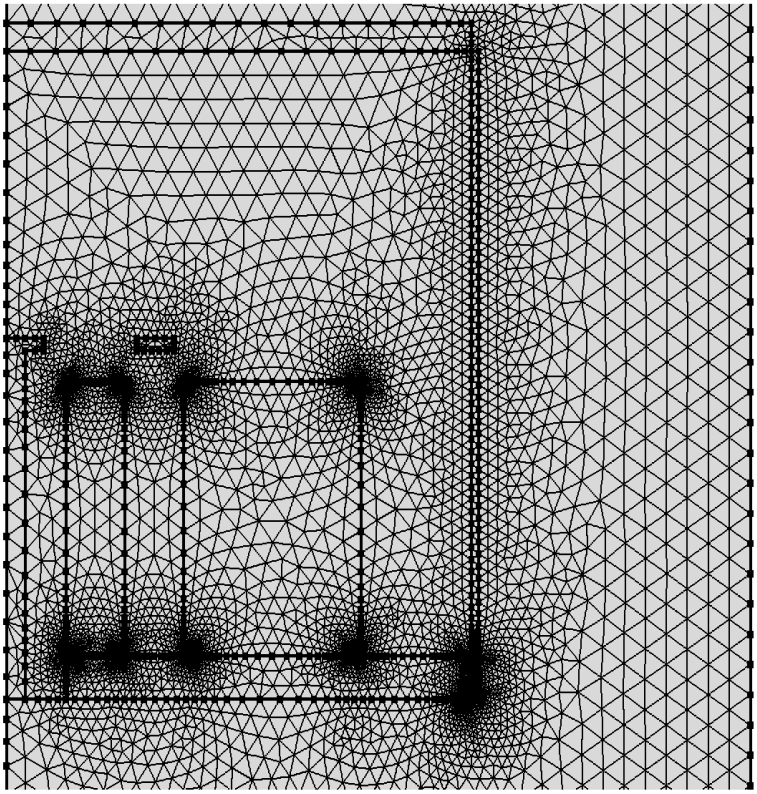

Figure 5-9. Finer meshing of antenna geometry

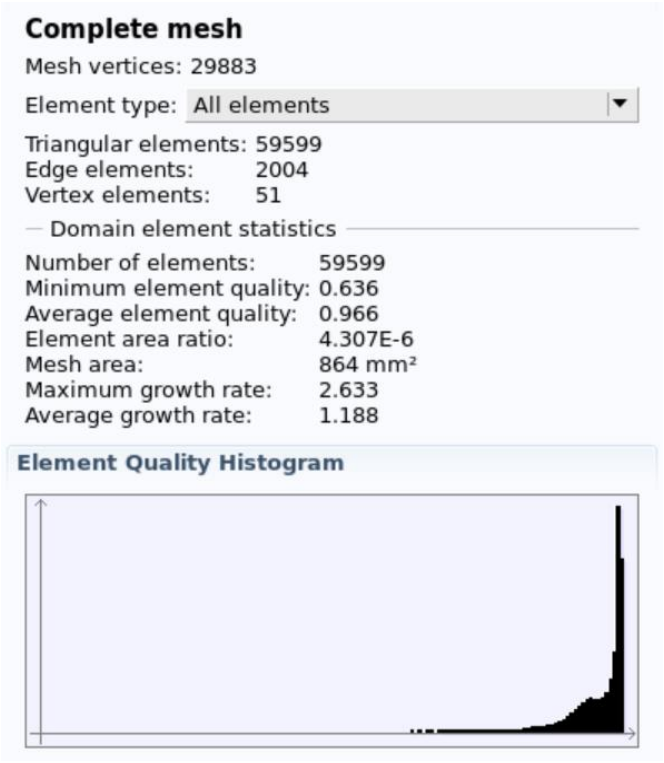

Figure 5-10. Antenna mesh quality

5.2.2.5 Solver

A solver is selected manually to override the default method provided by COMSOL Multiphysics. Here the GMRES is selected as an iterative preconditioning method. This is like its variant mentioned in the magnetic field simulation and uses a Multigrid as the preconditioner. Figure 5-11 shows the iteration process running about five times before starting to converge in finer segments.

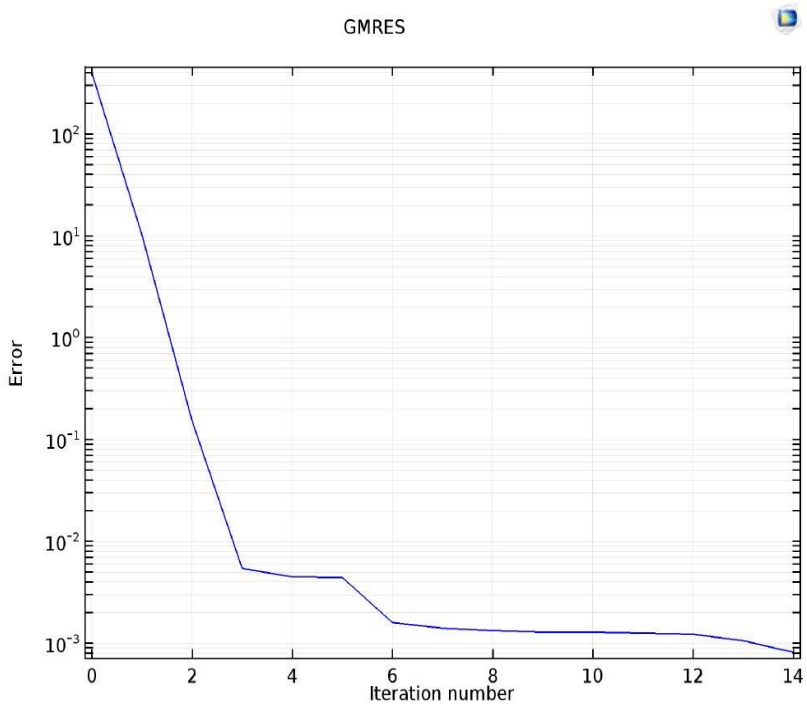

Figure 5-11. GMRES convergence

5.2.2.6 Results

Figure 5-12 shows the ECR frequency range after the implementation of the ring antenna and the respective changes in the ECR region is shown in Figure 5-13. This is crucial to validating the placement and orientation of the ring antenna to efficiently generate and sustain plasma by ensuring the optimal interaction between the electric and magnetic field

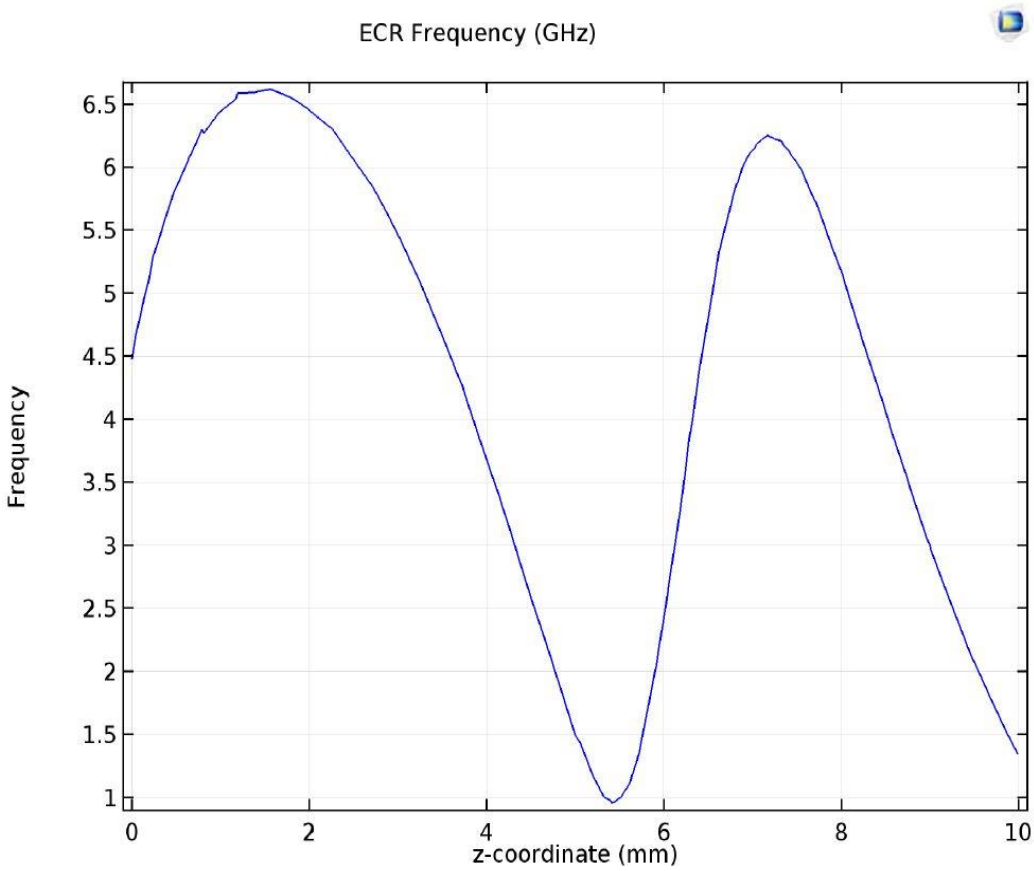

Figure 5-12. ECR frequency range with antenna

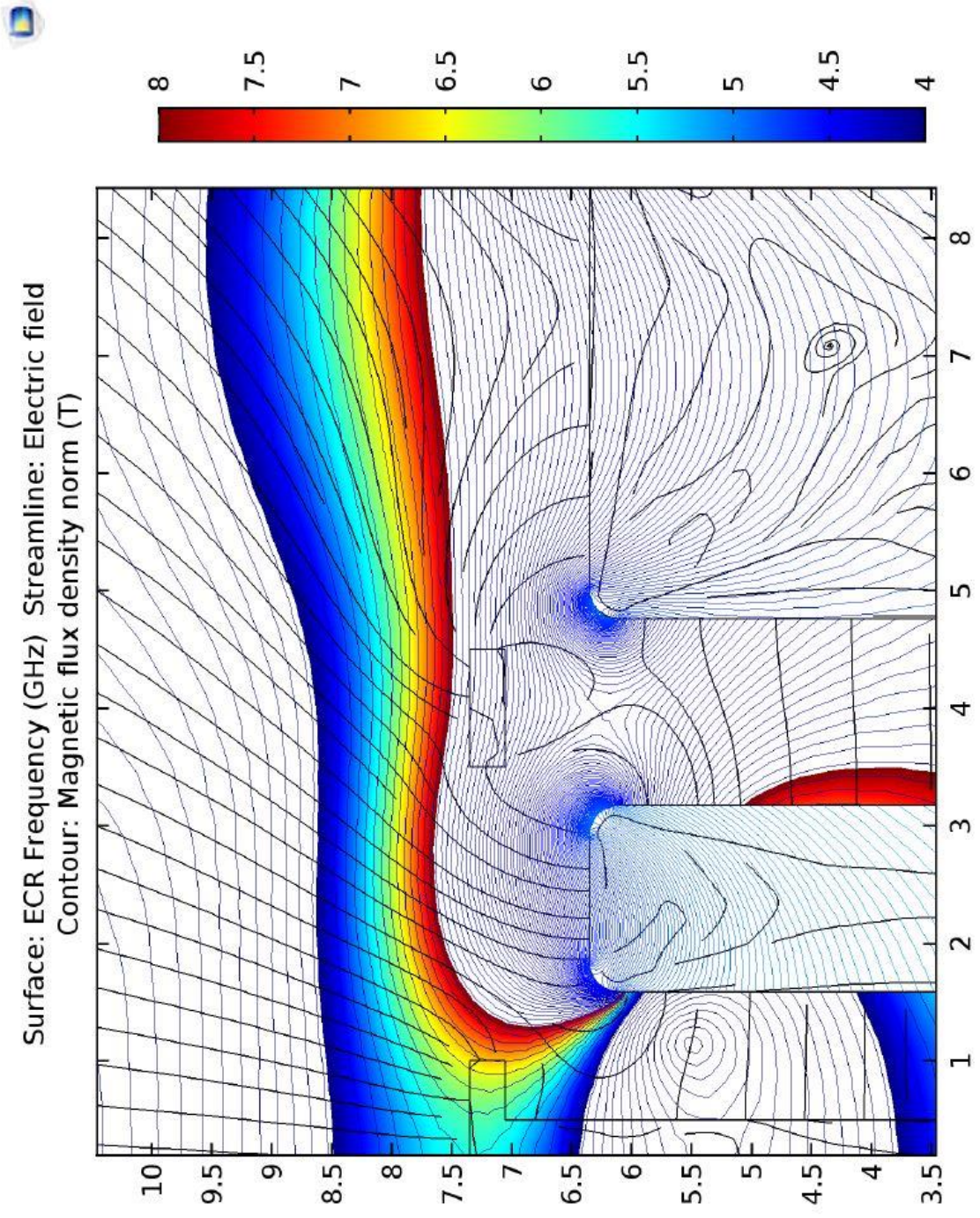

Figure 5-13. ECR region

5.3 Experimental Results with the New Design

The changes made to the thruster design overviewed in thesis have reduced the input power requirements for the thruster operation, decreased the reflected power, and demonstrated beam extraction. These changes were made considering the previous numerical simulation data and the current experimental research, which has indicated a need for orientation changes to the antenna and magnets. The log–mag plots of the reflected power (S_{11}) over the operating frequency range for the previous and latest version of the MMIT are shown in Figure 5-14 and Figure 5-15 respectively. The new design shows better results after the changes were implemented along with appropriate changes made to the microwave tuning setup to account for better impedance matching. Both the plots show resonance at around 4.9 GHz, but the new design keeps reflections below −40 dB, rather than −20 dB for the previous iteration.

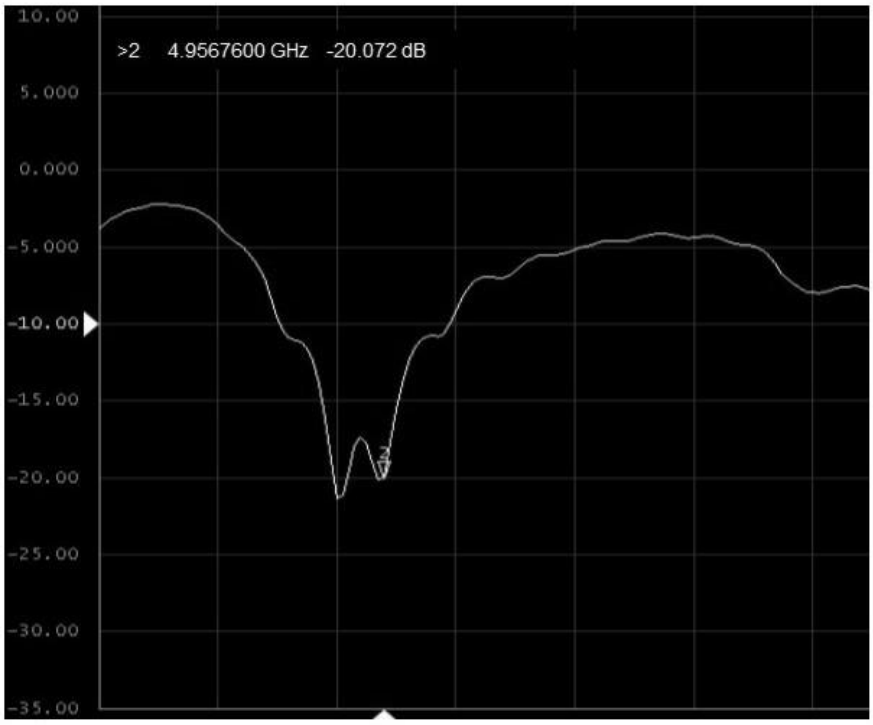

Figure 5-14. S_{11} plot of the previous design

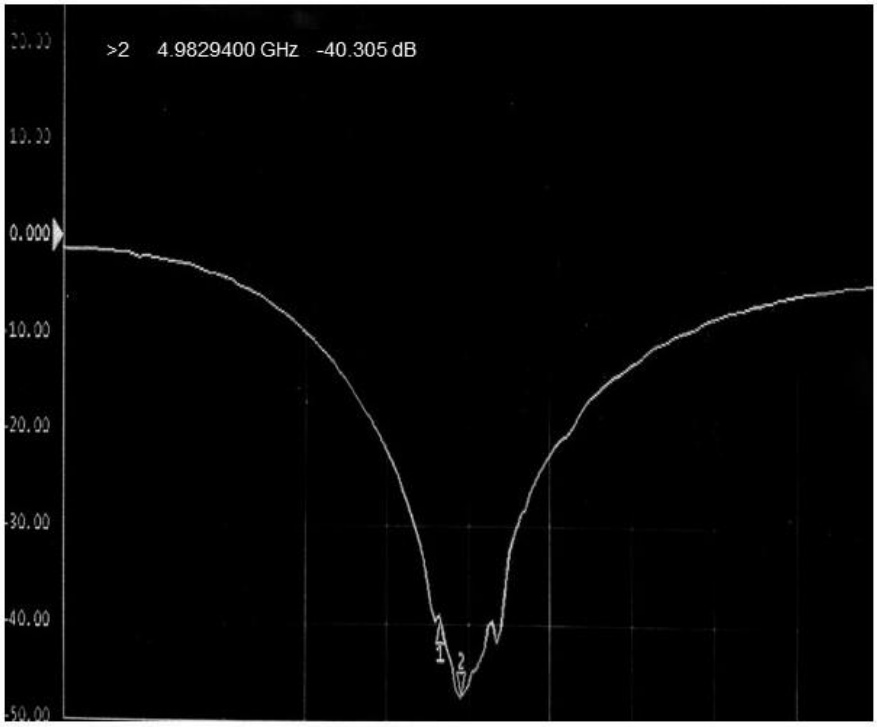

Figure 5-15. S_{11} plots of the latest design

The new design has been successful in generating plasma at input powers as low as 2.6–3.3 W with only 0.1 W power required to sustain plasma once ignited (power requirements fluctuate due to the minor differences in setup for each experiment). These variations in input power requirements are expected to be reduced as the thruster progresses to a more stable experimental version and ultimately the flight version.

Initial testing of this version of the MMIT produced arcing between the grids and between the screen grid and the antenna. Occasionally, the arc would jump from the acceleration grid over to the rear section of the thruster. This was a destructive process when generating plasma and attempting extraction. Several grids and antennas had to be replaced due to sputtering of plasma on the surfaces and other damages from arcing. The outer arc shown in Figure 5-16 was a result of a design flaw in shaping the grid connectors with squared extensions, which caused arcing from the corners.

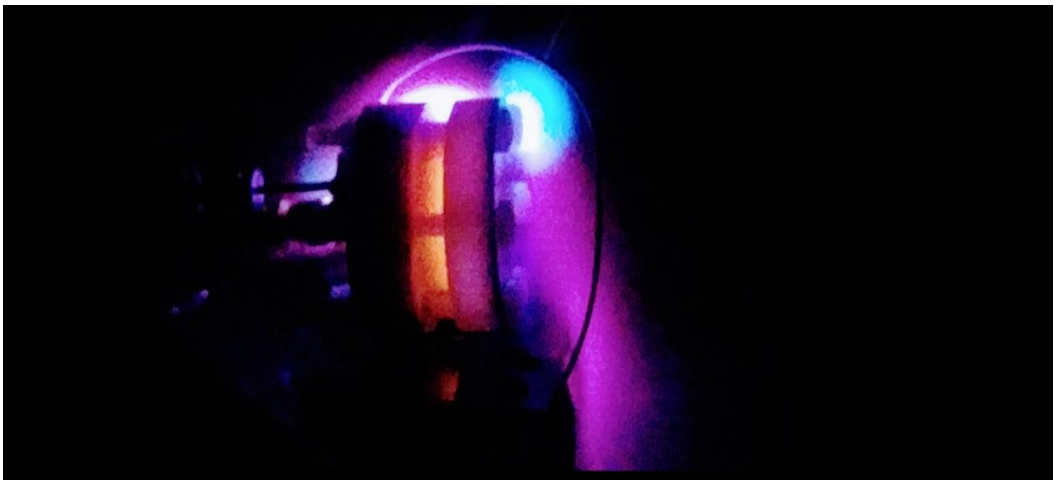

Figure 5-16. Arcing during an attempt at extracting the ion beam

The spacers were also deformed due to arcing damage and an accumulation of sputtered material from the initial round of testing. These were problems that existed in the previous design and had to be mitigated to obtain the first successful ion beam extraction shown in Figure 5-17.

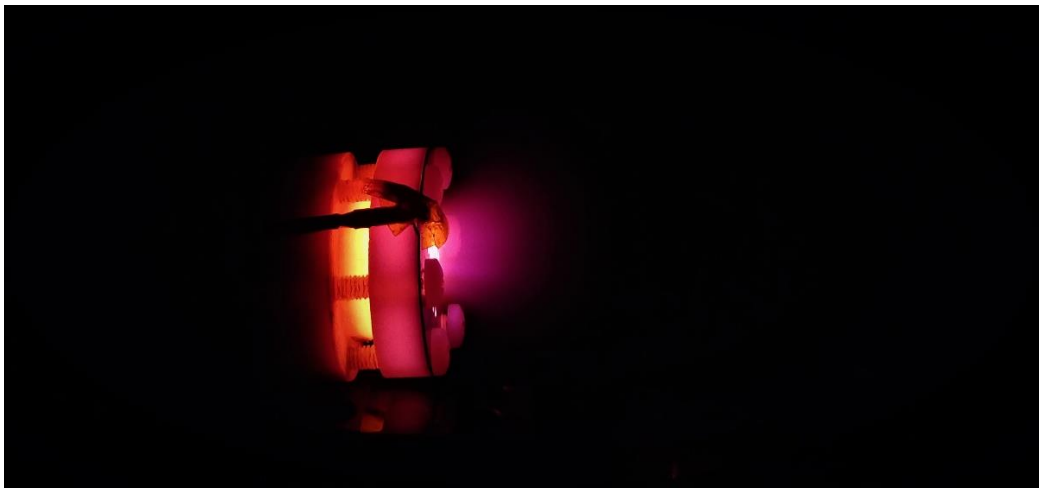

Figure 5-17. First successful ion beam extraction

The initial arcing problems were resolved by eliminating sharp edges in the design and using Kapton insulation to serve as a redundancy in case of deformations due to unaccounted errors.

Figure 5-18 shows the grids after the first set of experiments to determine the nature and severity of the arcing problem. Although running the arc test was a destructive process, it served as a way of revealing leaks in the system during the postprocessing of data, allowing these problems to be successfully eliminated.

Figure 5-18. Extraction grid set after arc testing

The experimental procedures involved testing the generation of plasma at different mass flow rates ranging from 0.1 sccm to 0.3 sccm. The power requirements for generating and sustaining plasma were found by incrementing the input power at a rate of 0.2 W (for generation) and decreasing the power at a rate of 0.1 W (for sustainment) until the plasma dies. The characteristics of the plume were analyzed by using the Langmuir probe to acquire the necessary data to calculate thrust, specific impulse, and efficiency. The calculations were made based on the equations provided in Chapter 2. To limit the complexity of our calculation, we combined certain variables into ratios to help make changes in the system with fewer complications in the processing of our data.

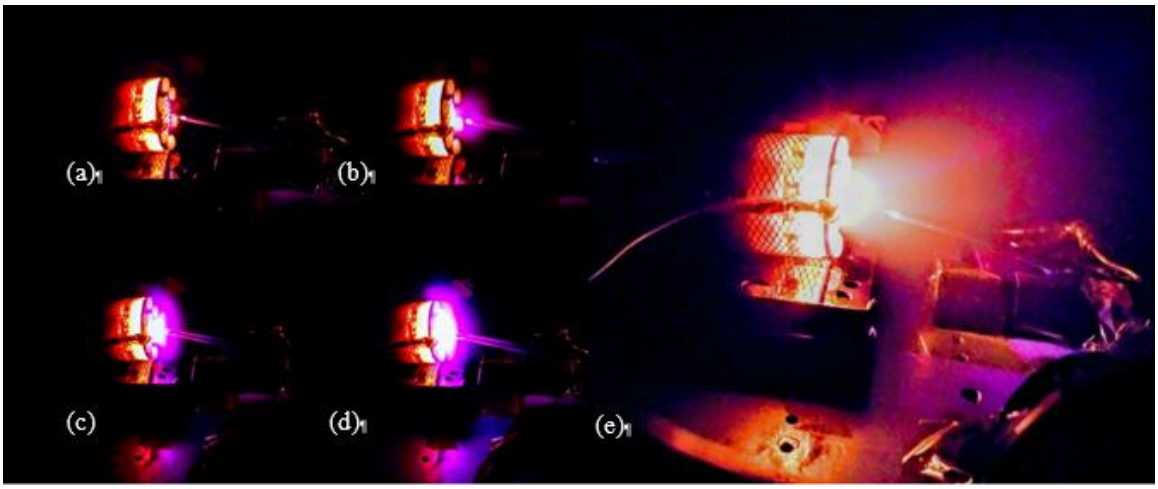

Figure 5-19. Exhaust plume under various throttle settings

The ion beam currents were measured as shown in Figure 5-19 by using the Langmuir probe placed a few centimeters away from the grids. Exhaust plume under various throttle settings were observed; (a) shows the thruster operating at zero throttle; (b) and (c) are intermediate; and (d) at the maximum experimental throttle before breakdown occurs. We observe that, with changes in the throttle setting coupled with the difference in input power, we clearly have different ionization levels at (e) as indicated by the visual changes in the plume. To fully characterize the behavior of the ion beam characteristics and determine the level of ionization in the system will require further analysis.

The values shown in Table 5-4 are the projected and experimental values for specific impulse at different mass flow rates. The results shown in Table 5-4 and Figure 5-20 indicate a specific impulse of 2470 s and thrust of 0.1 mN at 0.25 sccm mass flow rate of argon with total efficiency of 36 % at 3.3 W of input power. Lowering the mass flow requirement would increase the total efficiency and specific impulse of the thruster at a similar range of thrust. Although the efficiency and specific impulse are lower than the projected values, further optimization should allow us to reach targeted thrust, specific impulse, and efficiency by the next iteration of the MMIT.

Table 5-4. Mass Flow Rate vs. Specific Impulse

	Mass Flow Rate (sccm)	**Thrust (mN)**	**I_{sp} (s)**
Projected	0.15	0.10	4080
Experimental	0.25	0.10*	2470*
Experimental	0.15	0.063*	2570*

*Calculated from experimental data

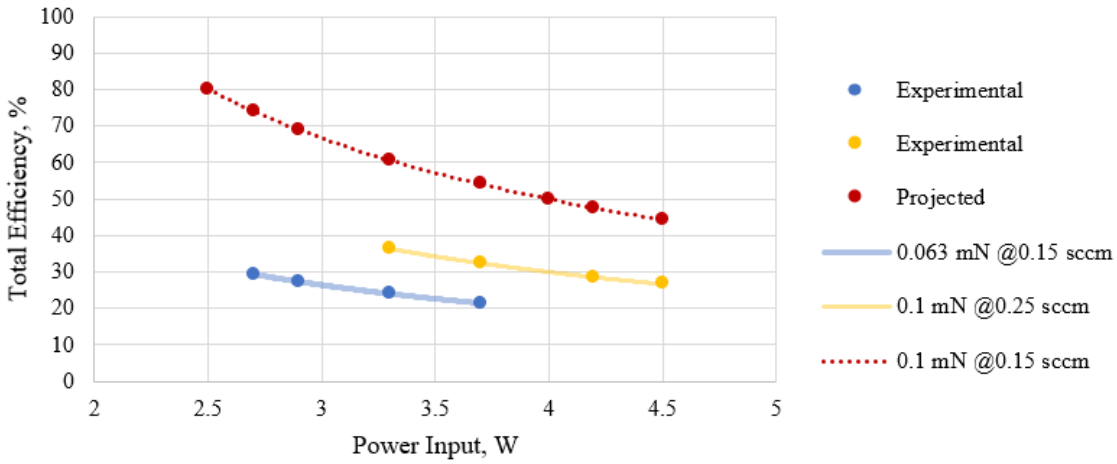

Figure 5-20. Input power vs. total efficiency.

Chapter 6

Conclusion and Future Work

A successful MMIT prototype has been designed and significant improvements to the MMIT's operation have been demonstrated. The current MMIT version uses a microwave ring antenna with neodymium permanent magnets to create plasma via an ECR discharge with the addition of a Faraday cage. This updated version has demonstrated extraction of the ion beam, which was a major issue with the previous version. We presented calculations based on experimental values for exhaust velocity, thrust, specific impulse, and efficiency. The work done on the MMIT has been an iterative process between experimental and computational research. Each iteration has brought us closer to the desired end goal of the MMIT project, which is to build a fully functional flight thruster suitable for applications on microspacecraft, such as CubeSats. There are four aspects that have played a key role in optimizing the microwave circuit for the thruster: antenna design, orientation, and position; installation of a Faraday cage; tuning the microwave setup using the double-stub tuner; and eliminating arcing. Experimental results at 4.9 GHz show calculated thrust values in the range of 0.06 mN to 0.10 mN with a specific impulse ranging from 2500 seconds to approximately 4500 seconds. The propellant used is argon at flow rates of 0.15 sccm to 0.25 sccm with input microwave power as low as 2.6 W for creating plasma and 0.1 W for sustaining the plasma. Even though the current efficiency is lower than the estimated value, we expect to be able to increase it in the next MMIT iteration which is currently being developed by the research team at The Pennsylvania State University.

Future work towards the development of a flight version of the MMIT would require further verification and validation through the iterative process between necessary simulations and experimental research.[56,57] This iterative process is crucial in converging towards a flight version of the MMIT.

The flight version of the MMIT should consider the use of xenon as propellant. The yoke plate would be made of iron and the permanent magnets would be made of samarium–cobalt (Sm–Co). The Faraday cage is to be redesigned to fit around the discharge chamber using a fine aluminum mesh and ceramic should be considered for making the discharge chamber.

The extraction grids should be made of molybdenum and the aperture array should be chemically etched or optically etched with lasers. Further testing on the heating effect[58] on the magnets due to the ECR plasma generation is required to estimate the life and functionality of the thruster under ideal operation conditions. This will allow us to design better systems towards the flight version of the MMIT.

A particle-in-cell simulation[59,60] of the plasma environment inside the thruster along with the numerical simulations of the ion and electron impingement on the extraction grids is crucial to design an optimal extraction system. This will effectively improve the focusing of the beam and maximize the transparency ration of the extraction grids.

Bibliography

[1] Administrator, N. C., "Glenn Contributions to Deep Space 1," *NASA* Available: http://www.nasa.gov/centers/glenn/about/history/ds1.html.

[2] Koizumi, H., and Kuninaka, Hi., "Low Power Micro Ion Engine Using Microwave Discharge," American Institute of Aeronautics and Astronautics, 2008.

[3] Kuninaka, H., Nishiyama, K., Shimizu, Y., Funaki, I., Koizumi, H., Hosoda, S., and Nakata, D., "Hayabusa Asteroid Explorer Powered by Ion Engines on the way to Earth," *Proceedings of the 31st Intern. Electric Propulsion Conferce, Ann Arbor, MI*, 2009.

[4] Nishiyama, K., Nakai, T., and Kuninaka, H., "Performance Improvement of the Microwave Discharge Ion Thruster u20," American Institute of Aeronautics and Astronautics, 2006.

[5] Conversano, R., and Wirz, R., "CubeSat Lunar Mission Using a Miniature Ion Thruster," American Institute of Aeronautics and Astronautics, 2011.

[6] Asif, M., Bilén, S. G., and Micci, M. M., "Prototyping and Optimization of a Miniature Microwave-Frequency Ion Thruster," *35th International Electric Propulsion Conference*, Georgia Institute of Technology, USA: 2017, pp. 1–8.

[7] Sengupta, A., Anderson, J. A., Garner, C., Brophy, J. R., Groh, K. D., Banks, B., and Karniotis, T. A., "Deep Space 1 Flight Spare Ion Thruster 30,000-Hour Life Test," *Journal of Propulsion and Power*, vol. 25, Jan. 2009, pp. 105–117.

[8] Koizumi, H., and Kuninaka, H., "Ion Beam Extraction and Electron Emission from the Miniature Microwave Discharge Ion Engine μ1," *International Electric Propulsion Conference, IEPC-2009-178*, 2009.

[9] Takao, Y., Masui, H., Miyamoto, T., Kataharada, H., Ijiri, H., and Nakashima, H., "Development of Small-Scale Microwave Discharge Ion Thruster," *Vacuum*, vol. 73, Apr. 2004, pp. 449–454.

[10] Yamamoto, N., Kataharada, H., Chikaoka, T., Masui, H., Nakashima, H., and Takao, Y., "Effect of Antenna Configuration on Thrust Performance in a Miniature Microwave Discharge Ion Engine," *29th International Electric Propulsion Conference, Princeton University, Princeton, NJ*, 2005.

[11] Takao, Y., Kataharada, H., Miyamoto, T., Masui, H., Yamamoto, N., and Nakashima, H., "Performance Test of Micro Ion Thruster using Microwave Discharge," *Vacuum*, vol. 80, Sep. 2006, pp. 1239–1243.

[12] Trudel, T. A., Bilén, S. G., and Micci, M. M., "Design and Performance Testing of a 1-cm Miniature Radio-Frequency Ion Thruster," *31st Internationational Electric Propulsion Conference, IEPC*, 2009, pp. 20–24.

[13] Mistoco, V. F. M., "Modeling of Small Scale Radio-Frequency Inductive Discharges for Electric Propulsion Applications," Doctor of Philosophy, The Pennsylvania State University, 2011.

[14] Lubey, D. P., Bilén, S. G., Micci, M. M., and Taunay, P.-Y., "Design of the Miniature Microwave-Frequency Ion Thruster," *Proc. 32nd Int. Electr. Propuls. Conf.*, 2011, pp. 1–8.

[15] Taunay, P.-Y., "Testing and Optimizaton of a Miniature Microwave Ion Thruster," 2012.

[16] Taunay, P.-Y. C., Bilén, S. G., and Micci, M. M., "Numerical Simulations of a Miniature Microwave Ion Thruster," *33rd Int. Elect. Propuls. Conf., Washington, DC, USA*, 2013.

[17] Lubey, D. P., "Development of A Miniture Microwave-Frequency Ion Thruster," 2011.

[18] "NASA - The Tyranny of the Rocket Equation" Available: https://www.nasa.gov/mission_pages/station/expeditions/expedition30/tryanny.html.

[19] Hill, P. G., and Peterson, C. R., *Mechanics and Thermodynamics of Propulsion*, Addison-Wesley, 1992.

[20] Jahn, J., Robert G., *Physics of Electric Propulsion*, McGraw-Hill, 1968.

[21]"Equivalent Exhaust Velocity – Liquid Rocket Engines (J-2X, RS-25, general)" Available: https://blogs.nasa.gov/J2X/tag/equivalent-exhaust-velocity/.
[22]Goebel, D. M., and Katz, I., *Fundamentals of Electric Propulsion: Ion and Hall Thrusters*, John Wiley & Sons, 2008.
[23]Sutton, G. P., and Biblarz, O., *Rocket Propulsion Elements*, John Wiley & Sons, 2016.
[24]Kaufman, H. R., *An Ion Rocket with an Electron-Bombardment Ion Source*, Washington, D.C. :, 1961.
[25]Leiter, H., Ellerbrock, H., Berger, M., Boss, M., Feili, D., Lotz, B., and Di Cara, D., "Development of a Miniaturized RF Ion Engine System for Commercial and Scientific applications," American Institute of Aeronautics and Astronautics, 2011.
[26]Leiter, H. J., Killinger, R., Bassner, H., Müller, J., Kukies, R., and Fröhlich, T., "Development and Performance of the Advanced Radio Frequency IonThruster RIT-XT," p. 9.
[27]Kuninaka, H., and Satori, S., "Development and Demonstration of a Cathodeless Electron Cyclotron Resonance Ion Thruster," *Journal of Propulsion and Power*, vol. 14, Nov. 1998, pp. 1022–1026.
[28]Sercel, J., "Electron-Cyclotron-Resonance (ECR) Plasma Acceleration," American Institute of Aeronautics and Astronautics, 1987.
[29]Funaki, I., Kuninaka, H., and Toki, K., "Plasma Characterization of a 10-cm Diameter Microwave Discharge Ion Thruster," *Journal of Propulsion and Power*, vol. 20, Jul. 2004, pp. 718–727.
[30]"K&J Magnetics - Specifications" Available: https://www.kjmagnetics.com/specs.asp.
[31]"Table of Properties for SmCo Magnets" Available: http://www.magnetsales.com/SMCO/Smcoprops.htm.
[32]"Magnetic Materials" Available: http://www.permagsoft.com/english/assets/applets/Materials.pdf.
[33]"Alnico Magnet Grades - Available Grades of Alnico Magnets | Dura Magnetics USA" Available: https://www.duramag.com/alnico-magnets/available-alnico-magnet-grades/.
[34]Yamamoto, N., Kondo, S., Chikaoka, T., Nakashima, H., and Masui, H., "Effects of Magnetic Field Configuration on Thrust Performance in a Miniature Microwave Discharge Ion Thruster," *Journal of Applied Physics*, vol. 102, Dec. 2007, p. 123304.
[35]Kamis, Y. E., and Celik, M., "Study of the Discharge Chamber Magnetic Field Configuration Effects on the Electron Cyclotron Resonance (ECR) Microwave Ion Thruster," American Institute of Aeronautics and Astronautics, 2015.
[36]Yamamoto, N., Chikaoka, T., Masui, H., Nakashima, H., Takao, Y., and Kondo, S., "Magnetic Field Design in Miniature Microwave Discharge Ion Engines," American Institute of Aeronautics and Astronautics, 2006.
[37]Nakayama, Y., Funaki, I., and Kuninaka, H., "Sub-Milli-Newton Class Miniature Microwave Ion Thruster," *Journal of Propulsion and Power*, vol. 23, Mar. 2007, pp. 495–499.
[38]"CTI Cryo-Torr 10 Vacuum Pump" Available: http://www.idealvac.com/product.asp?pid=4451.
[39]"Keysight / Agilent / HP 8481A Power Sensor" Available: http://www.bellnw.com/manufacturer/Agilent/8481A.htm.
[40]"E4419A EPM Series Dual-Channel Power Meter" Available: https://www.keysight.com/en/pd-1000002799%3Aepsg%3Apro/epm-series-dual-channel-power-meter?cc=US&lc=eng.
[41]Stanford Research Systems, "Series PS300 High Voltage Power Supplies - User Manual," 2000, 2004, 2007 1998.
[42]Newport, "Oriel 70705 High Voltage Power Supply - Datasheet" Available: https://www.artisantg.com/info/ATGpmqhw.pdf.
[43]mks, "ALTA Series True Digital Mass Flow Meter/Controller - Instruction Manual," 2006.
[44]Sercel, J., and Fitzgerald, D. J., "ECR plasma Thruster Research - Preliminary Theory and Experiments," American Institute of Aeronautics and Astronautics, 1989.

[45]Pozar, D. M., *Microwave Engineering*, Hoboken, NJ: Wiley, 2012.
[46]Balanis, C. A., *Advanced Engineering Electromagnetics*, John Wiley & Sons, 2012.
[47]Steer, M., *Microwave and RF-Design*, Scitech Publishing, 2013.
[48]Tabatabaian, M., *COMSOL® 5 For Engineers*, 2015.
[49]Pryor, R. W., *Multiphysics Modeling Using COMSOL®: A First Principles Approach*, 2011.
[50]Pryor, R. W., *Multiphysics Modeling Using COMSOL and MATLAB*, 2016.
[51]Coring Incorporated Lighting & Materials, "MACOR®" Available: https://media.freeola.com/other/11763/macor_pdf.pdf.
[52]Rosenberg, S. J., *Nickel and its Alloys*, 1968.
[53]"Dielectric Constants of Various Materials" Available: http://www.clippercontrols.com/pages/Dielectric-Constant-Values.html.
[54]"Generalized Minimal Residual Method," *Wikipedia*, Mar. 2018.
[55]Morikuni, K., Reichel, L., and Hayami, K., "FGMRES for Linear Discrete ill-Posed Problems," *Applied Numerical Mathematics*, vol. 75, Jan. 2014, pp. 175–187.
[56]Tsukizaki, R., Koizumi, H., Nishiyama, K., and Kuninaka, H., "Plasma Diagnostics inside the ECR Ion Thruster u 10 by Laser Absorption Spectroscopy with Optical Fiber Probes," American Institute of Aeronautics and Astronautics, 2012.
[57]Okumura, S., Arakawa, K., Fukuda, M., Nakamura, Y., Yokota, W., Ishimoto, T., Kurashima, S., Ishibori, I., Nara, T., Agematsu, T., Sano, M., and Tachikawa, T., "Magnetic Field Stabilization by Temperature Control of an Azimuthally Varying Field Cyclotron Magnet," *Review of Scientific Instruments*, vol. 76, Mar. 2005, p. 033301.
[58]Tsukizaki, R., Nishiyama, K., and Kuninaka, H., "Electron Heating Model in μ10 Ion Thruster," *35th International Electric Propulsion Conference*, Georgia Institute of Technology, USA: 2017.
[59]Wang, J., "Three-Dimensional Particle Simulations of NSTAR Ion Optics," p. 12.
[60]Takao, Y., Koizumi, H., Komurasaki, K., Eriguchi, K., and Ono, K., "Three-Dimensional Particle-in-Cell Simulation of a Miniature Plasma Source for a Microwave Discharge Ion Thruster," *Plasma Sources Science and Technology*, vol. 23, Dec. 2014, p. 064004.